

Mineralogy of Terra Meridiani and western Arabia Terra from OMEGA/MEx and implications for their formation

F. Poulet^{a,*}, R.E. Arvidson^b, C. Gomez^a, R.V. Morris^c, J.-P. Bibring^a, Y. Langevin^a,
B. Gondet^a, J. Griffes^{b,d}

^a Institut d'Astrophysique Spatiale, Université Paris-Sud, 91405 Orsay Cedex, France

^b Department of Earth and Planetary Sciences, Washington University, St. Louis, MO 63130, USA

^c NASA Johnson Space Center, Houston, TX 77058, USA

^d Center for Earth and Planetary Studies, National Air & Space Museum, Smithsonian Institution, Washington, DC 20013, USA

Received 25 January 2007; revised 22 October 2007

Available online 19 January 2008

Abstract

Analyses of Mars Express OMEGA hyperspectral data (0.4–2.7 μm) for Terra Meridiani and western Arabia Terra show that the northern mantled cratered terrains are covered by dust that is spectrally dominated by nanophase ferric oxides. Dark aeolian dunes inside craters and dark streaks extending from the dunes into the intercrater areas in mantled cratered terrains in western Arabia Terra have similar pyroxene-rich signatures demonstrating that the dunes supply dark basaltic material to create dark streaks. The dissected cratered terrains to the south of the mantled terrains are dominated spectrally by both low-calcium and high-calcium pyroxenes with abundances of 20–30% each retrieved from nonlinear radiative transfer modeling. Spectra over the hematite-bearing plains in Meridiani Planum are characterized by very weak but unique spectral features attributed to a mixture of a dark and featureless component (possibly gray hematite) and minor olivine in some locations. Hydrated minerals (likely hydrous ferric sulfates and/or hydrous hydroxides) associated with poorly ferric crystalline phases are found in the etched terrains to the north and east of the hematite-bearing plains where erosion has exposed ~ 1 km of section of layered outcrops with high thermal inertias. These materials are also found in numerous craters in the northern Terra Meridiani and may represent outliers of the etched terrain materials. A few localized spots within the etched terrain also exhibit the spectral signature of Fe-rich phyllosilicates. The ensemble of observations show that the evidence for aqueous processes detected by the Opportunity Rover in Meridiani Planum is widespread and confirms the extended presence of surface or near-surface water over this large region of Mars. The scenarios of formation of Terra Meridiani (“dirty” acidic evaporite, impact surge or weathering of volcanic ash) cannot satisfactorily explain the mineralogy derived from the OMEGA observations. The formation of the etched terrains is consistent with leaching of iron sulfides and formation of sulfates and hydrated iron oxides, either in-place or via transport and evaporation of aqueous fluids and under aqueous conditions less acidic than inferred from rocks examined by Opportunity.

© 2007 Elsevier Inc. All rights reserved.

Keywords: Mars, surface; Mineralogy; Spectroscopy

1. Introduction

The purpose of this paper is to use OMEGA (Observatoire pour la minéralogie, l’eau, les glaces et l’atmosphère) hyper-spectral data to provide mineralogical compositions for the surface of Terra Meridiani and Arabia Terra, focusing on the

etched terrains as mapped by Hynek et al. (2002) and Arvidson et al. (2003). The study area straddles the prime meridian from 10° W to 10° E longitude, 5° S to 15° N latitude (Fig. 1) and includes the classical low-albedo Sinus Meridiani and the southern part of Arabia Terra, where large exposures of layered sedimentary rock occur in numerous locations (Malin and Edgett, 2000). The regional geological context for the study area has been carefully described in numerous papers using imaging and spectra from Mars Global Surveyor (MGS) and Mars Odyssey observations. Arvidson et al. (2003) mapped four different

* Corresponding author.

E-mail address: francois.poulet@ias.u-psud.fr (F. Poulet).

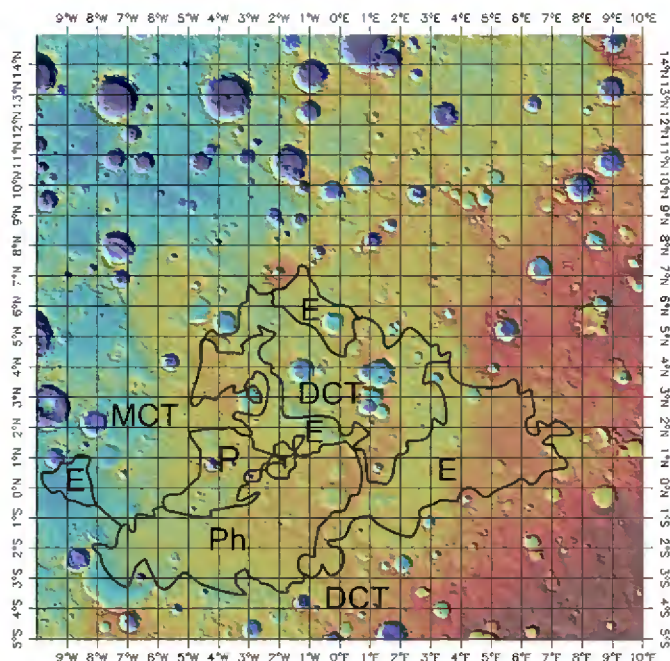


Fig. 1. Color-coded shaded relief from MOLA data from 0 to -3 km of the study area. The boundaries of the geologic units are shown (Arvidson et al., 2003): E = etched unit, Ph = hematite-bearing plains, MCT = mantled cratered terrains, DCT = dissected cratered terrains, P = plain unit.

units: (1) Noachian cratered terrains, referred to as Dissected Cratered Terrain (DCT) unit because of extensive dissection by channel systems, (2) hematite-bearing plains unit (referred to as unit Ph, for Plains Hematite identified by the MGS/Thermal Emission Spectrometer; Christensen et al., 2000, 2001); the northwestern edge of the Ph unit was mapped by Arvidson et al. (2003) as a plains unit, called unit P, although additional mapping by us in this paper shows that it is in fact the DCT unit, (3) a thick stack (~ 1 km) of layered light-toned deposits called Etched terrains (termed unit E by Hynek et al., 2002) directly beneath the Ph unit and deposited onto the unit DCT; the unit E terrains are inferred to have significant proportions of rocks because high thermal inertias (Arvidson et al., 2003; Hynek, 2004); and (4) towards the north, the three units are covered by a mantle that was mapped as Mantled Cratered Terrain (MCT) unit.

The MCT unit represents a part of the heavily cratered terrain of Arabia Terra where light-toned layers can be traced (Edgett and Parker, 1997; Edgett, 2002). Many craters in this area have wind-eroded, horizontally bedded deposits on their floor (Edgett, 2002). These layered outcrops are most common and more extensive in craters closest to Terra Meridiani. Several origins have been proposed for the deposits in Arabia Terra, including paleopolar, volcanoclastic, eolian, and subaqueous sedimentary processes (Scott and Tanaka, 1986; Schultz and Lutz, 1988; Edgett and Parker, 1997; Chapman and Tanaka, 2002; Hynek et al., 2002; Edgett and Malin, 2002). This region also exhibits numerous dark streaks originating from barchan dune fields in craters, with an uncertain source material (Edgett, 2002).

The study area includes the Opportunity Mars Exploration Rover landing site in Meridiani Planum (MER-B) located near 1.94° S, 5.56° W in the Ph unit. The first navigation camera images received from Opportunity showed that the rover landed on low albedo surface material superposed on an eroded, light-toned and layered rock (Squyres et al., 2004). Further analysis demonstrated that the rocks were sedimentary and the hematite detected by remote sensing was associated with a lag deposit of hematitic granules released during the physical breakdown of the light-toned bedrock, which is enriched in sulfates. Geochemical models indicate that the mineralogy inferred for Meridiani outcrop rocks compares closely with that expected during the evaporative evolution of waters formed during sulfuric acid weathering of olivine basalt (Squyres and Knoll, 2005). Other formation processes that have been proposed to explain the presence of sulfates in the outcrops include deposition of volcanic ash followed by reaction with condensed SO_2 and H_2O from fumaroles (McCullom and Hynek, 2005) and deposition from a ground hugging turbulent flow of rocks and ices produced by meteorite impact (Knauth et al., 2005). It has been also argued that the outcrops are the upper layers of unit E (Hynek, 2004; Arvidson et al., 2006). So far, the rover team has used Opportunity to explore several meters of stratigraphic section exposed in the walls of the Eagle, Endurance, Erebus, and Victoria craters. Compared to sedimentary rock exposures located elsewhere in the Terra Meridiani region, the outcrops explored by the rover cover a very small area, typically too small to resolve from orbit using the OMEGA instrument.

A campaign of coordinated observations between Opportunity and several orbiters was conducted over the past three years. Recent analysis of observations acquired by the Mars Express OMEGA instrument indicate that the rover traverse regions are dominated by pyroxene, plagioclase feldspar, gray hematite, and dust, consistent with Pancam, Mini-TES, and Mössbauer observations, although olivine detected in basaltic soil by Mössbauer (Morris et al., 2006) was not evident in OMEGA spectra (Arvidson et al., 2006). OMEGA data covering the etched terrains not visited by Opportunity show enhanced water bands at $\sim 1.9 \mu\text{m}$ (Gendrin et al., 2005) and, in some localities, evidence for the presence of kieserite ($\text{MgSO}_4 \cdot \text{H}_2\text{O}$) and polyhydrated magnesium sulfate minerals (Arvidson et al., 2005; Griffes et al., 2007). From the combined analysis of observations from OMEGA and Opportunity, Arvidson et al. (2006) proposed the following scenario for formation of the Meridiani regional deposits: "The most plausible regional-scale is one in which the water table rose relative to the dissected cratered terrain surfaces, resulting from tectonic subsidence and/or enhanced recharge of the cratered terrain highlands to the southwest... Sulfur and other volatile species were introduced to the hydrologic system as a consequence of extensive volcanism from Tharsis (and other) volcanoes and/or by weathering of pre-existing sulfur-bearing deposits and would have produced an acid sulfate groundwater system."

Although numerous ground and orbital data sets over the study area have been analyzed, several key questions relevant

Table 1
Spectral parameters used in this study for mapping the minerals. $R(\lambda)$ is the reflectance at the wavelength λ (μm). The parameterization and the detection threshold are discussed in Poulet et al. (2007) and in Section 2.1

Name	Formulation	Detection threshold	Rationale
Pyroxene	$1 - (R(2.15) + R(2.22))/(R(1.81) + R(2.49))$	0.01	2 μm band due to both low-calcium and high-calcium pyroxene
Olivine	$(0.5 * R(1.69) + 0.5 * R(1.70))/(0.1 * R(1.01) + 0.1 * R(1.21) + 0.4 * R(1.36) + 0.4 * R(1.50))$	1.02	1 μm band due to olivine
0.55 μm band depth or Fe^{3+}	$1 - R(0.55)/(0.5 * R(0.44) + 0.5 * R(0.65))$	0	Ferric minerals and oxidation state
0.97/0.80 ratio	$R(0.97)/R(0.80)$	1	Nanophase ferric oxides
1.35/1.0 slope	$(R(1.34) + R(1.36))/(R(1.00) + R(1.01))$	1.10	Poorly crystalline ferric phases
1.9 μm band depth	$1 - R(1.93)/(0.5 * R(1.83) + 0.5 * R(2.12))$	0.02	Water-bearing minerals
2.30 μm band depth	$1 - R(2.30)/(0.25 * R(2.26) + 0.25 * R(2.27) + 0.5 * R(2.34))$	0.02	Metal-OH feature indicator of Fe/Mg-rich clays

to better understanding the origin of the sedimentary rocks in Terra Meridiani and Arabia Terra and placing the rocks at the Opportunity site into regional context have not been addressed until now. How is the surface mineralogical composition correlated with the geologic units? Is the surface composition uniform inside a given unit? Are key minerals such as phyllosilicates present in the study area? What are the relationships between the deposits identified in the craters of Arabia Terra and the layered material detected over Terra Meridiani? Is there a compositional connection between dark streaks and layered units found within the craters? Is the surface composition of the etched terrains consistent with the formation of the outcrops observed at Opportunity as an evaporite brine? Is the mineralogy of the entire region consistent with the scenario of formation proposed by Arvidson et al. (2006)?

This paper focuses on a spectroscopic study from remote sensing observations acquired by OMEGA. In order to address the posed questions, the mineralogical composition and correlations with geomorphologic and stratigraphic properties at different scales are emphasized.

2. Methodology

2.1. Spectral parameters

We analyze the OMEGA visible to near-infrared (VNIR) reflectance spectra (0.4 to 2.5 micrometers) using orbital data sets through orbit 1999 (January 2004 to October 2005 or $L_s = 330^\circ$ – 300°). The orbits cover most of the study area at different spatial resolutions (~ 350 m to 2 km) depending on spacecraft altitude. Data were limited to spectra that do not exhibit aerosol water ice absorption bands. In addition, a number of quality parameters in the OMEGA database were used to eliminate anomalous data, including non nadir-pointing observations, saturated data, and spectra containing spurious values. Bibring et al. (2004) describe details of the instrument, and Poulet et al. (2007) discuss data reduction procedures. Langevin et al. (2007) investigated the signal to noise ratio of the instrument: it exceeds 50 for most of the C channel and part of the visible channel and can reach values of several hundreds for the C channel depending on albedo and illumination conditions.

To map surface mineralogy, a series of spectral criteria were developed in Poulet et al. (2007) to cover a broad range of materials: band depth of the 2 μm pyroxene feature, band depth of the 0.53 μm ferric absorption feature, a nanophase ferric oxide spectral criterion based on the ratio of the reflectance at 0.97 and 0.8 μm , an olivine index based on the 1 μm band, and band depth at 1.9 μm indicative of the presence of H_2O -bearing minerals. These parameters have been carefully described in terms of parameterization and detection thresholds in Poulet et al. (2007). Two additional spectral indexes related to the identification of ferric components and phyllosilicates were developed and used in this paper. We next review some of these parameters and all summarize them in Table 1.

- (a) The identification of olivine from the OMEGA spectra is based on the increase of the reflectance in the 1.1–1.7 μm range, which results from overlapping absorptions centered near 1 μm . As presented in Poulet et al. (2007), two spectral parameters can be used: one is sensitive to the forsterite end-member, and the other is sensitive to fayalite end-member and/or with larger grain size. In this paper the olivine distribution was mapped using the second criterion, which is less affected by false positives.
- (b) The spectra of many ferric minerals are characterized by:
 - (i) an absorption edge between 0.4 and ~ 0.75 μm with an inflection or “kink” near 0.55 μm ,
 - (ii) a shallow absorption band, normally visible as a shoulder, between ~ 0.6 and ~ 0.75 μm ,
 - (iii) a reflectance maximum at ~ 0.75 μm ,
 - (iiii) an absorption band centered at ~ 0.85 to 0.95 μm giving a rise in reflectance up to ~ 1.3 – 1.4 μm .
 Three of these spectral signatures are used to narrow the mineralogical composition of the ferric components as follows:
 - (b1) Band depth at 0.55 μm (also called Fe^{3+} parameter), which is related to the strength of the ferric absorption edge, and a plot of this criterion against many laboratory samples can be found in Morris et al. (2000).
 - (b2) Ratio of reflectance at 0.97 μm relative to the value at 0.8 μm . Most ferric weathering products are characterized by band with a minimum centered between 0.80 and 1.0 μm with a depth that depends on the crystallinity and with a position that varies with the mineralogical composition (Morris et al., 1989, 1997,

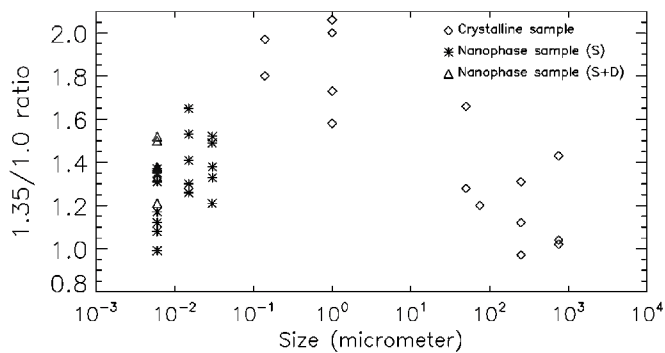


Fig. 2. Values of the 1.35/1.0 slope parameter for a set of hematite samples of different grain sizes (from Morris et al., 1989). All the samples are red in the NIR as can be noted by the values larger than 1. The values are maximal for the fine-grained (smaller than a few μm), bright red hematite sample (samples HMS3, HMS10, HMS12, HMS13, HMS14, and HMS15, in lozenge). By contrast, the particulate samples (10–90, 90–500, 500–1000 μm) of hematite samples HMMG1, HMIR2 and WD039 (in lozenge) are gray in color with values close to 1 for the largest grain size samples. For comparison, nanophase hematite samples (samples S6FN1-6, S15FN1-5, S30FN1-5, type D and S6FN25, type S + D) plot in a region of intermediate values.

2000). Unfortunately, the OMEGA visible channel does not have a good enough signal to noise in the 0.8–1.0 μm interval to discriminate between the different ferric minerals (Bellucci et al., 2006). The magnitude of the slope from 0.8 to $\sim 1 \mu\text{m}$ is still useful in characterizing the ferric phase because it is highly dependent on the crystallinity of the ferric phases (Morris et al., 1989). For hematite, the 0.97/0.80 reflectance ratio is the strongest for grain sizes between several hundreds of nanometers and several tens of micrometers and becomes shallow for larger grain sizes. In specular hematite, the band is shallow but still present (Lane et al., 2002). For grain sizes smaller than a few tens of nanometers (the so-called nanophase ferric oxides) spectra exhibit a distinct convex shape between 0.8 and 1.0 μm . As a test, the 0.97/0.8 μm spectral parameter has been calculated for the laboratory samples of hematite particles smaller than 10 nm (samples S6FN-type D from Morris et al., 1989) and typical values ranged between 1.0 and 1.05 were obtained. Values close to or slightly larger than 1 can indicate the presence of nanophase ferric oxides.

- (b3) Ratio of reflectance at 1.35 versus 1.0 μm , which provides information about the iron content and the degree of crystallinity of ferric phases (Morris et al., 1989). The ratio is maximal for poorly crystalline mineral (grain size smaller than 1 μm in the case of hematite for instance) as shown in Fig. 2. This parameter is therefore used to map this unique spectral characteristic, whose origin will be discussed depending on the presence or not of a 0.9 μm band. By taking a detection threshold larger than 1.1, the martian bright regions that exhibit the typical nanophase ferric oxides signatures are not mapped because they have values of about 1.0–1.05. In Bibring et

al. (2007), this spectral parameter was also used to map the ferric oxides at a planetary scale and the results were consistent with two other mapping methods (Modified Gaussian Model and linear unmixing).

- (c) The presence of water molecules in surface materials is inferred using the $\sim 1.9 \mu\text{m}$ band depth. This feature results from a combination of fundamental vibrations of H_2O molecule ($\nu_2 + \nu_3$). The 1.9 μm band has been detected by OMEGA in very few places (Bibring et al., 2005), usually in association with a sharp cation-OH band in phyllosilicates or water in sulfate lattices (Bibring et al., 2005; Poulet et al., 2005; Gendrin et al., 2005). The 1.9 μm band is interpreted as indicative of the presence of hydrated phases such as hydrated phyllosilicates, hydrated sulfates, and hydrous hydroxides. We note that some phyllosilicates [e.g., kaolinite $\text{Al}_2\text{Si}_2\text{O}_5(\text{OH})_4$] are not hydrated and neither are simple oxyhydroxides (e.g., goethite FeOOH) because they do not contain H_2O molecules. Some sulfates (e.g., kieserite, romerite), are excluded in this mapping because the hydration band of these minerals is shifted to longer wavelengths (Cloutis et al., 2006). Other minerals such as szomolnokite, coquimbite, mirabilite also exhibit a broad absorption band near 2.1 μm (McCord et al., 2001; Cloutis et al., 2006) which can nevertheless contribute to mapping of the 1.9 μm band.
- (d) In order to look for phases having M–OH (M = Fe and Mg) bands, a spectral index using the absorption band centered near 2.30 μm was defined (Table 1). This spectral feature, if present along with a the 1.9 μm band, is attributed to Fe/Mg-rich phyllosilicates (Clark et al., 1990; Bishop et al., 2002; Poulet et al., 2005). A threshold of 0.02 is used in order to be significantly above instrumental noise that is around 1.5%. Visual inspection of individual spectra from different regions was always done to confirm that the spectral signature of the cation-OH feature can be reliably detected under a wide range of observing conditions (solar illumination, atmospheric dust opacity, state of the instrument, etc.) when the index is > 0.02 .

Spectral parameters have not been developed for important minerals such as gray hematite and feldspar, because they are spectrally featureless in the OMEGA wavelength range. However, their presence influences both the continuum and the overall reflectance magnitude, as well as shapes and band depths for other minerals, so that a nonlinear spectral unmixing method as described below and careful spectral signature analyses provide constraints on their presence and relative abundances.

2.2. Nonlinear spectral modeling

One of the significant challenges for the use of reflectance spectroscopy for retrieving mineral composition and abundance is quantifying the relationships between the band depth of spectral features and mineral abundances and mineral grain sizes. In this work, we use the approach adopted by Shkuratov et al.

(1999). This approach is based on a geometrical optics approximation, as is the more familiar Hapke model (1981), and is used to transform optical constants and grain size information into a reflectance spectrum for a particulate material. Poulet et al. (2002) showed its degree of realism and efficiency relative to other scattering models (e.g., the Hapke model and its derivatives). The model has been also tested to determine the type of mixture (sand, areal, or bedrock), the relative proportions, and the grain sizes of components of laboratory mineral samples (Poulet and Erard, 2004), as well as applied to spectra of several planetary surfaces (Poulet and Cuzzi, 2002; Poulet et al., 2002, 2003; Arvidson et al., 2006). For each spectrum the model must satisfy two major constraints: the depth and the shape of the absorption(s) band(s) and the average value of the reflectance. One additional free parameter was used to modestly adjust the continuum spectral slope resulting from aerosols and/or photometric effects. The data were fit using a simplex minimization algorithm (Nelder and Mead, 1965).

Although nonlinear modeling of OMEGA reflectance spectra is a powerful way to explore data sets, the method has limitations. First, the set of optical constants used as end-members must be representative of materials that are under study. Because we will apply the method to low albedo regions that are dominated by basaltic materials, the minerals used in this paper are a low-calcium pyroxene (pigeonite: RELAB sample PP-EAC-042) a high-calcium pyroxene (diopside: RELAB sample PP-CMP-027), a Fe-rich olivine [fayalite; collected by G. Bonello (personal communication)], a Mg-rich olivine (forsterite: RELAB sample PO-CMP-032), a feldspar (labradorite: SPECLIB sample ts02b), and a dark oxide (magnetite: USGS sample HS78). The optical constants were derived using the scheme described in Poulet and Erard (2004) from reflectance spectra and detailed again in Arvidson et al. (2006). Second, the end-members must be spectrally distinct in order to recover the proper mineral abundances and mineral grain sizes. Feldspars are spectrally featureless in the NIR, so that the spectral modeling can lead to non-unique solutions for grain size and abundances of this component. Because the observations of the martian surface by MGS-TES have demonstrated that the plagioclase is a major component of low albedo regions (Bandfield, 2002), this component is included as an end-member. Third, the spectral modeling is highly nonlinear and uses radiative transfer calculations that are very time consuming. Consequently, this procedure is restricted to analysis of selected spectra.

3. Regional surface mineralogy

3.1. Mafic mineral mapping and nonlinear unmixing

3.1.1. Pyroxene

A map of the pyroxene index is given in Fig. 3. The spatial distribution is well correlated with low albedo regions (namely the unit DCT) the eastern part of the P unit (now believed by us to be dominantly DCT), and most of the dark deposits inside and outside (dark streaks) craters in Arabia Terra. It is interesting to note that for a given dark streak, the pyroxene

signature is higher in the interior of the crater than in the dark streak and it is not found over the entire streak. The dark streak emanating from the crater at 7° N, 6.9° E is a good example, where no pyroxene is mapped over a part of the dark streak (Fig. 4). Based on a set of synthetic spectra, we investigated the detection threshold for the pyroxene spectral index in term of abundance, and we found that a pyroxene concentration of 5% or more with grain size of 100 μm intimately mixed with dust would be detected. Low albedo regions of Mars usually exhibit pyroxene signatures (Poulet et al., 2007). Given the very low albedo of the Ph unit, we expected to identify pyroxene with OMEGA. However, only a few areas of the unit Ph show positive pyroxene detection.

Our mineral nonlinear unmixing model has been applied to two spots selected because of their high pyroxene band depths: 8.52° E, 4.35° S and 359.11° E, 2.44° N. The surface spectra and best fit models are compared in Fig. 5, and the derived grain size and mineral abundances are given in Table 2. The fits are rather good with Residual Mean Squared lower than 0.002 (Table 2), indicating that no spectrally important component is missing. The primary mineral is plagioclase, although the abundance is uncertain for this component by at least 10% based on previous experience (e.g., Poulet et al., 2002, 2003). Increasing the grain size could be compensated by a decrease of the abundance of plagioclase, testimony to the lack of uniqueness of the models resulting from the spectrally flat nature of the data. Both High-Calcium Pyroxene (HCP) and Low-Calcium Pyroxene (LCP) are required to fit the surface composition of the DCT terrains. The model fit became highly degraded (Fig. 5) when low-calcium pyroxene was removed as a component, demonstrating the sensitivity of the model to the mineral. The identification of LCP over the DCT unit is in good agreement with the first OMEGA results on the spatial distribution of LCP, which show that it is preferentially found in the ancient Noachian-aged units (Mustard et al., 2005). The grain sizes derived for the pyroxene components (50–500 μm) are in the range of the sand-size particles. The derived surface properties are therefore in favor of a surface covered by basaltic sands. This is consistent with many eolian features (dunes) visible on MOC images, which reveals mobile material by wind.

Finally, we note that olivine is not required to model the DCT spectra. The detection limit of olivine in the OMEGA spectra was studied in Poulet et al. (2007). An olivine concentration of 5% or more with grain size of 100 μm would give a fairly straightforward detection. By contrast, olivine with a grain size of 10 μm is not detectable below concentration of 15%. Therefore, the presence of olivine at a low concentration (less than 15%) cannot be excluded in the DCT unit. We remark that the derived composition is very different from that obtained from the modeling of TES spectra (Arvidson et al., 2003). In particular, the large amount of alteration products found (phyllosilicates as much as 25%) is not consistent with the results of our analyses. Our retrieved mineralogy is more consistent with the latest TES-based analysis of the DCT surface mineral composition done by Rogers and Christensen (2007). In particular, they found no evidence of alteration product such

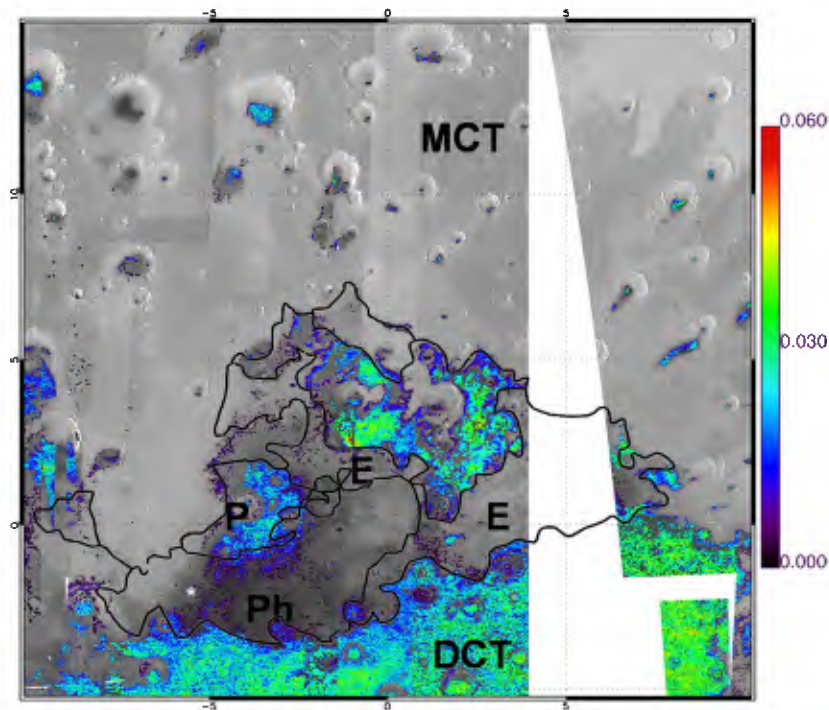


Fig. 3. Pyroxene index over the OMEGA map of the albedo at $1.08 \mu\text{m}$ with a range from black (10%) to light gray (45%). The color bar gives the values of the pyroxene spectral parameter (Table 1). Pixels with values below the detection limit (0%) are not plotted. The white asterisk indicates the location of the Opportunity landing site.

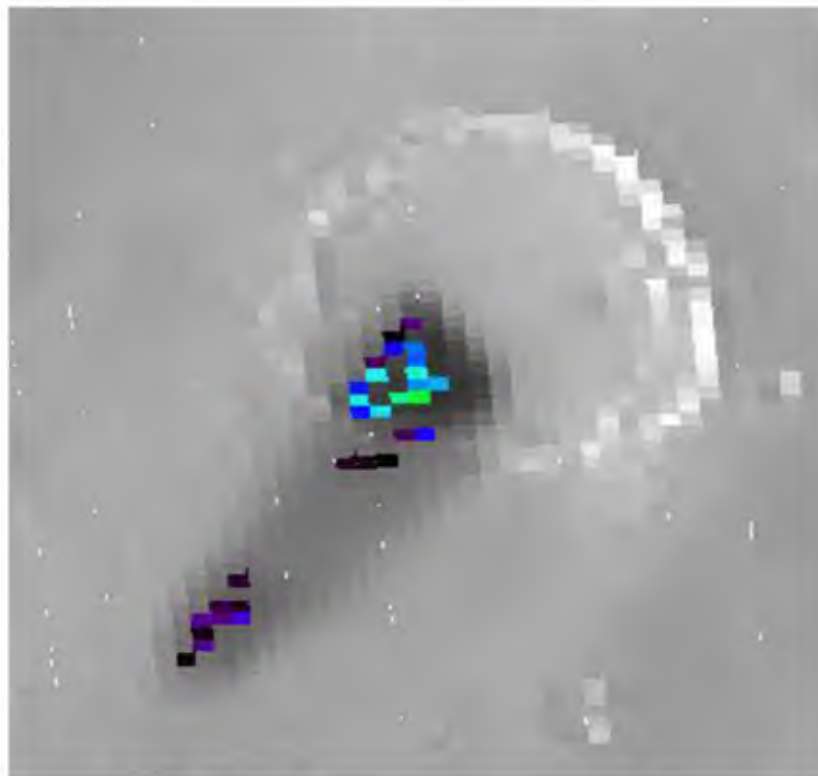


Fig. 4. Zoom of the pyroxene map over a dark streak emanating from the crater located at 7°N , 6.9°E . The gray scale corresponds to the albedo at $1.08 \mu\text{m}$ with a range from black (10%) to light gray (45%).

as phyllosilicates, and a mineral abundance of 22% for HCP. They also report the presence of LCP but at a lower concentration than OMEGA (a few percents in comparison to 20–30%

from OMEGA). A careful comparison between OMEGA and TES results for the low albedo regions of Mars is in preparation.

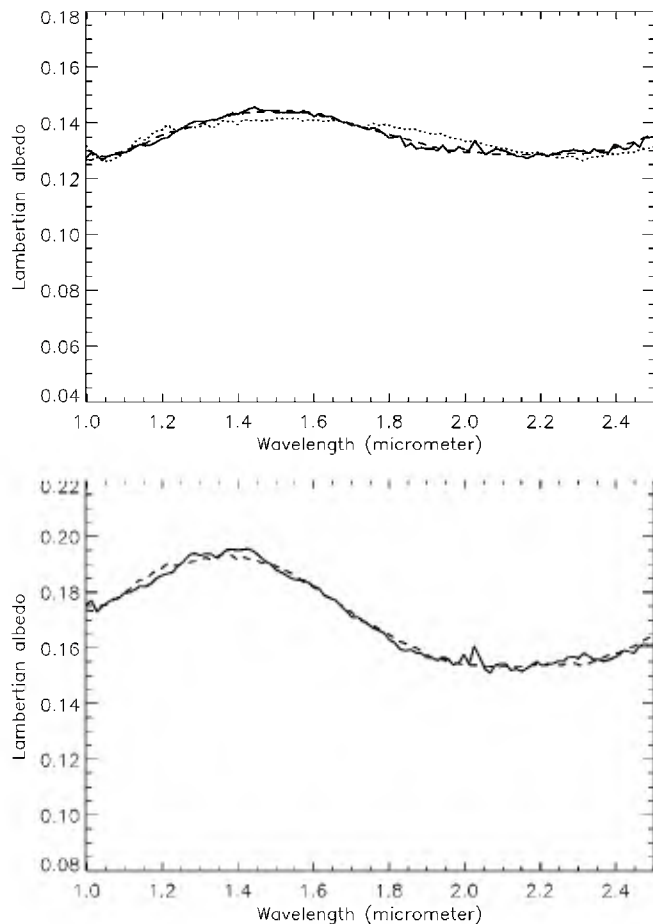


Fig. 5. Nonlinear unmixing models of two spectra extracted from the DCT unit. Upper: the observed spectrum (solid line) of the first spot is compared to two models: the best fit model (dashed line) and one model excluding the low-calcium pyroxene (dotted line). Lower: the observed spectrum (solid line) of the second spot is compared to its best model. The end-members and their corresponding size and abundance are listed in Table 2.

3.1.2. Olivine mapping

As shown in Fig. 6, the Ph unit shows a positive detection for olivine, with index values as high as 1.05, i.e. slightly above the detection limit set up at 1.02 discussed in Poulet et al. (2007). The olivine-rich unit (2–3° S, 356–358° E) cor-

relates well with the zone where the highest concentration of hematite was found (yellow-red zone of Plate 2 in Christensen et al., 2001). A deeper examination of the spectral properties is done by comparing the spectrum to an olivine-free terrain (Fig. 7). The ratio spectrum exhibits a strong rise up to 1.7–1.8 μm and the absence of a flat bottom, which can be best explained by the presence of iron-rich olivine with a fine-grain size ($<10 \mu\text{m}$). Both the albedo and the thermal inertia of this olivine-rich zone are lower than those of the plains traversed by Opportunity (Christensen et al., 2005).

OMEGA observations of the Opportunity landing site did not show spectral evidence for olivine (Arvidson et al., 2006), even though this mineral was clearly identified in Opportunity Mössbauer (Klingelhöfer et al., 2004; Morris et al., 2006) and Mini-TES (Christensen et al., 2004) data in the basaltic sands that cover the traverse sites. Arvidson et al. (2006) have noted that the non-identification of olivine over the landing site by OMEGA could be best explained by the specific backscattering properties of the olivine relative to other minerals and/or by preferential weathering of olivine surfaces.

3.2. Ferric phases mapping

Fig. 8 shows the diversity of the ferric band in the visible range and the Fe^{3+} index map is presented in Fig. 9. Note that the mapping shows some variations from orbit to orbit resulting from the atmospheric variations. This effect is expected because the strongest contribution of aerosols in terms of spectral signatures and quantitative effects occurs in the visible range. The lowest values of the Fe^{3+} index (about 8–10%) are found over the unit Ph, especially over the region where olivine and gray hematite have been detected by this work and Christensen et al. (2001). More specifically, the spectrum in the 0.5–0.8 μm region over the hematite-rich plain is characterized by the smallest Fe^{3+} band depth observed thus far at these spatial resolutions on Mars. This characteristic is unique on Mars and strongly suggests the presence of a dark and featureless component. Coarse-grained hematite ($>1 \text{ mm}$) that is gray in the visible (Lane et al., 2002) can explain the flat shape. The Fe^{3+} index calculated over the landing site area is about 20%

Table 2

Modal mineralogy for a nonlinear unmixing model of two regions located in DCT unit (see Section 3.1.1)

<i>Spot 1 (4.35° S, 8.52° E)</i>				
	<i>Model 1: Parameters free, RMS = 0.0011</i>			
	Diopside	Pigeonite	Plagioclase	Magnetite ^a
Grain size (μm)	450	20	100	–
Abundance (vol%)	30	30	36	4
	<i>Model 2: Pigeonite abundance forced to be zero, RMS = 0.0028</i>			
	Diopside	Pigeonite	Plagioclase	Magnetite ^a
Grain size (μm)	50	–	100	–
Abundance (vol%)	30	0	65	5
<i>Spot 2 (2.44° N, 359.11° E), RMS = 0.0018</i>				
	Diopside	Pigeonite	Plagioclase	Magnetite ^a
Grain size (μm)	300	50	10	–
Abundance (vol%)	30	20	45	5

^a Magnetite is included as small inclusions smaller than the wavelength.

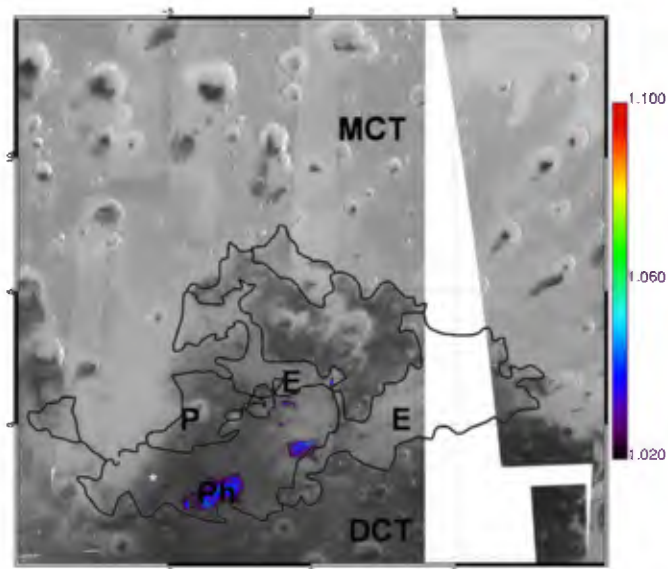


Fig. 6. Olivine index over the OMEGA map of the albedo at 1.08 μm with a range from black (10%) to light gray (45%). The color bar gives the values of the olivine spectral parameter (Table 1). Pixels with values below the detection limit (1.02) are not plotted. The white asterisk indicates the location of the Opportunity landing site.

larger than the lowest values found in the Ph unit. This observation coupled with the higher albedo at the landing site is best explained by a larger coverage of ferric dust. The unit MCT (except for the dark streaks) exhibits the highest values (between 25 to 35% of band depth). Intermediate values are found in the units E and DCT.

The values of the Fe^{3+} index can be used to constrain the mineralogy of the ferric phases (Morris et al., 2000). The observed positive ferric absorption is not consistent with the sulfate jarosite, because the band depth calculated from laboratory spectra indicates a parameter value of <0 . The values shown in Fig. 9 range between 0 and 0.3 can be assigned to a variety of Fe^{3+} -bearing minerals. Because increasing the band depth at 0.53 μm is a measure of increasing contribution of ferric oxides, the trend observed over the study area can be interpreted as a dominance by weakly altered basaltic materials for the low albedo unit Ph to basaltic sands with surface dusted with or coated by ferric-rich soil for the unit DCT to a ferric-rich surface for the unit MCT.

Mapping of the 0.97/0.8 ratio reveals regions with values close to or larger than 1, concentrated over bright regions and the MCT unit (red and white areas in Fig. 10). These values indicate the lack of NIR absorption (see spectra in Fig. 12), corresponding to the lack of a well-crystalline ferric mineral. The values of the Fe^{3+} and 0.97/0.80 spectral parameters exhibited by the unit MCT are consistent with the presence of a nanophase oxide (hereafter npOx) component, similar to what it is observed globally over bright regions of Mars. Note that the 0.97/0.8 μm ratio is much lower than 1 over the units Ph and DCT, which can be explained by the presence of ferrous minerals such as olivine and pyroxene for the hematite-bearing plains and pyroxene for the DCT terrains.

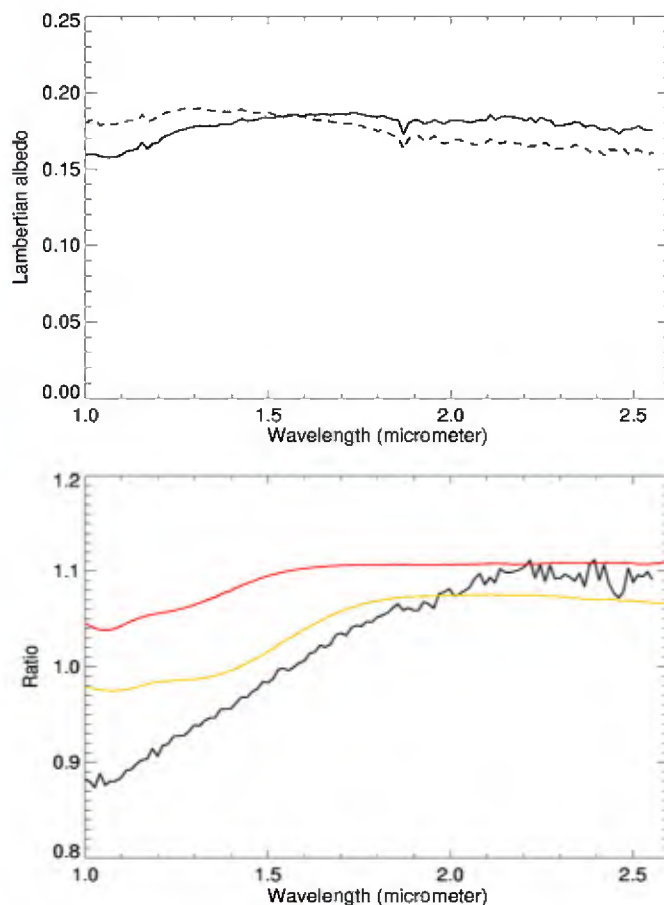


Fig. 7. Identification of olivine in the unit Ph. Upper: one olivine-rich spectrum (solid line) extracted from the Ph unit with a large value of the olivine index (Fig. 6) is compared to an olivine-free spectrum (dashed line). The spectra are corrected by the cosines of the incidence angles. Lower: ratio of the spectra and comparison with laboratory spectra of iron-rich olivine (red line) and Mg-rich olivine (yellow line) with grain size smaller than 45 μm . Olivine can best explain the strong increase in the 1.0–1.7 μm wavelength region.

Mapping of the 1.35/1.00 slope spectral parameter (Fig. 11) shows the index is larger than the detection threshold primarily for the unit E. The strong rise between 1 and 1.35 μm observed in the spectra of the etched terrains (Fig. 12) coupled with a deep 0.9 μm band in the visible part implies the presence of a crystalline ferric component as supported by numerous laboratory spectra published by Morris et al. (1989, 2000). Small patches are also mapped outside the unit E in some areas in the unit Ph and in some craters in the north of the unit E. By contrast, the lack of both a strong rise in the NIR and a 0.9 μm band in the spectrum of the bright unit MCT is in good agreement with a spectral dominance by nanophase ferric oxides (Figs. 10 and 12). Such spectral characteristics are common to most of the bright regions of Mars (Morris et al., 1997).

3.3. Hydrated minerals identification and mapping

3.3.1. Mineral identification

Terra Meridiani is one of a few regions where the 1.9 μm band has been detected on OMEGA-based maps at the plane-

tary scale (Poulet et al., 2007). The boundaries of the hydrated mineral-rich zones are abrupt and well correlated with unit E (Fig. 13). There are variations in the degree of the band depth inside the unit E, with index values ranging from 0 and 0.06. For instance, the northern and western parts of the unit E do not show evidence for hydration. We remark that these terrains have higher albedos and lower thermal inertias than the eastern part of the E terrains (Hynek, 2004). This suggests that the extent of hydration is related to the degree of induration and/or the rock abundance. Alternatively, it is possible that the spectral signature is being masked in high albedo low inertia areas because of a dust cover.

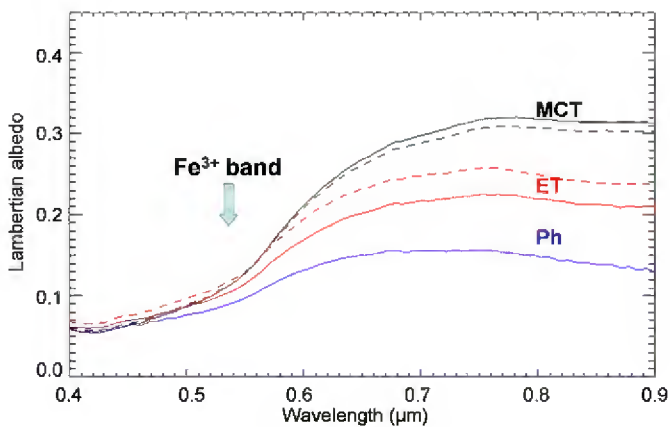


Fig. 8. Examples of spectra for each unit showing the spectral diversity in the visible range. Black dashed and solid lines: unit MCT. Red dashed and solid lines: unit ET. Blue solid line: unit Ph. Absorption in the 0.4–0.6 μm is characteristic of the Fe^{3+} signature measured by the 0.53 μm band depth. These 3 regions are spectrally pretty uniform in this wavelength range and the spectra have been selected to represent the diversity in term of albedo. Note that the S/N exceeds 50 in most part of the wavelength region.

Several occurrences of an enhanced 1.9 μm feature are also found inside craters located at the north of the unit E. A map of the 1.9 μm index for data from orbits at two different spatial resolutions (orbit 485, width swath of 128 pixels, $L_s = 44^\circ$ and orbit 1084, width swath of 16 pixels, $L_s = 118^\circ$) is given in Fig. 14. It is apparent from this map that the hydrated mineral index successfully detected hydrated mineral on the two orbits. This consistency provides confidence that the 1.9 μm index is a reliable indicator and that equivalent concentrations of relatively dust-free hydrated minerals do not exist elsewhere in the region except for the regions showing positive detection.

As noted in Section 2.1, the spectral feature at 1.9 μm is common to many water-bearing minerals such as hydrated sulfates, hydrous hydroxides and certain phyllosilicates. In some parts of the study area, this feature has been attributed to some Mg-bearing polyhydrated sulfates because a 2.4 μm feature is also present (Gendrin et al., 2005). The 1.9 μm criterion does not map the mono-hydrated sulfates (like the mineral kieserite) that were identified and mapped by their 2.1 and 2.4 μm bands (Arvidson et al., 2005, 2006; Gendrin et al., 2005; Griffes et al., 2007). These sulfate-rich terrains are located in the lower etched plains materials of the northern portion of Meridiani Planum (0° to 2° W and 1° to 2° N). We do not map them because they have been carefully studied in Griffes et al. (2007); for comparison with other regions, examples of spectra extracted from this region are however presented in Fig. 15 to show their distinctive nature.

A major question is whether or not phyllosilicate minerals can be detected within the study area. We use the 2.3 μm spectral criterion defined for mapping Fe/Mg-rich phyllosilicates. At a detection limit of 2% band depth, phyllosilicates are present in only two small spots inside a crater centered at 3.65° N, 0.9° W and inside the unit E located at 1.5° N,

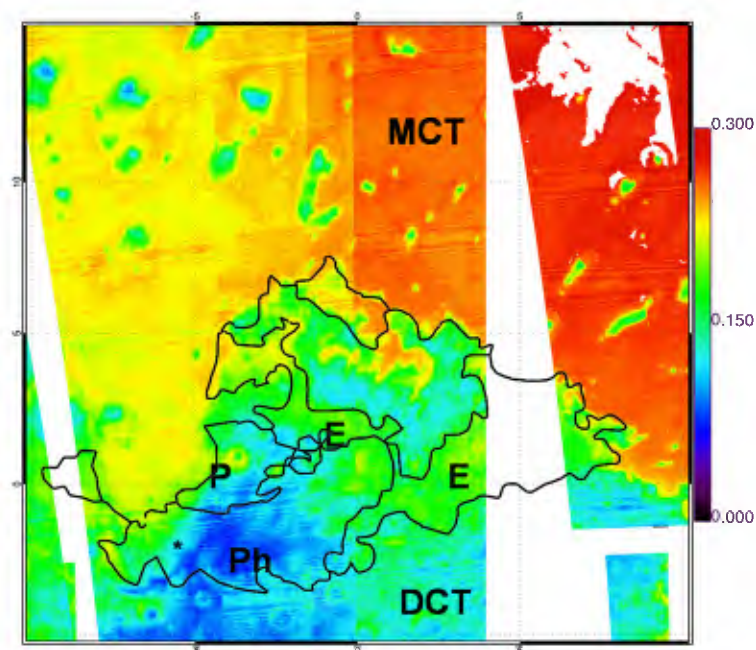


Fig. 9. Map of the at 0.53 μm band depth indicative of the presence of Fe^{3+} . The black asterisk indicates the location of the Opportunity landing site.

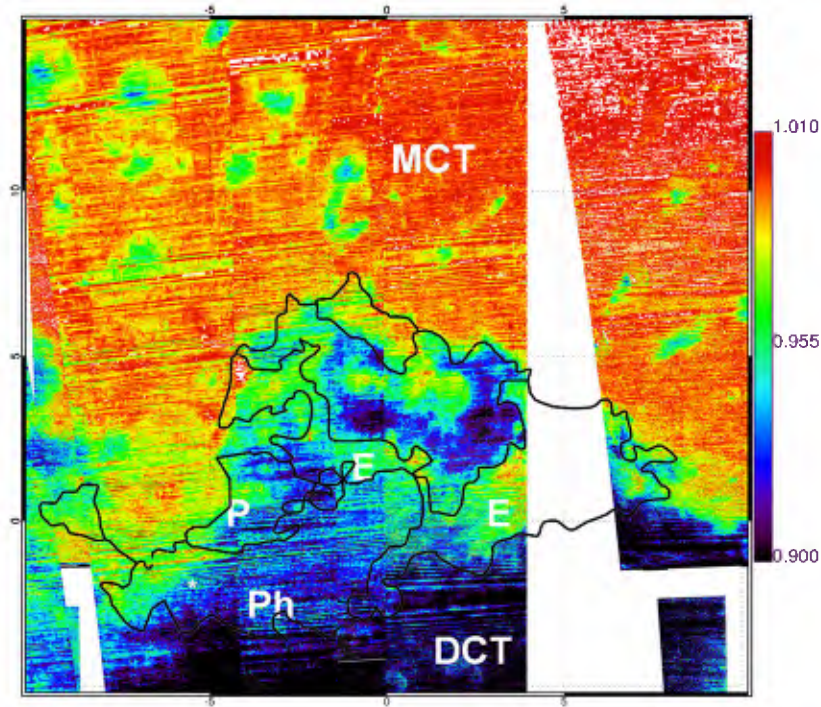


Fig. 10. Map of the nanophase oxide index. The stripes are instrumental artifacts due to a periodic noise (Bellucci et al., 2006). Colors that are above the scale are in white.

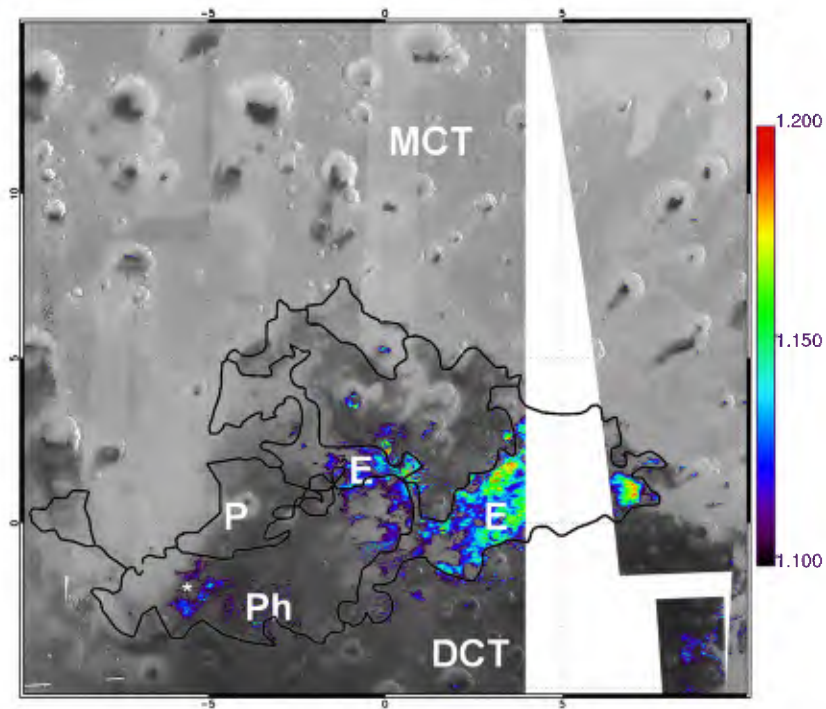


Fig. 11. Map of the spectral ratio 1.35/1.0 μm , indicator of the presence of poorly crystalline ferric minerals.

3.5° E (Fig. 16). This index has been computed for several orbits that passed through the two spots of interest and the identification was positive on all orbits. Inspection of individual spectra confirms that all the features typical of the Fe/Mg-rich phyllosilicates are reliably detected (Fig. 17). We note that the 2.3 μm signature is significantly weaker than that found

in the phyllosilicate-rich regions reported for other terrains on Mars (Poulet et al., 2005). Numerous factors can contribute to a weakening of this feature. In particular, a mixture with sulfates cannot be excluded because laboratory measurements done by Bishop et al. (1995) have shown that sulfate-bearing phyllosilicates can have spectral signatures similar to those of

pure phyllosilicates, but with weaker intensity. Small occurrences scattered along the unit E, especially in the eastern part are also visible in Fig. 15. However, these detections are uncertain because the values of the parameter are very close to the detection limit and the spatial distribution is scattered.

We note that there are sulfur-bearing species that are consistent with the spectral properties for unit E. Amaranthite, $\text{Fe}^{3+}\text{SO}_4\text{OH}\cdot 3\text{H}_2\text{O}$ has a 1.9 μm feature, while show-

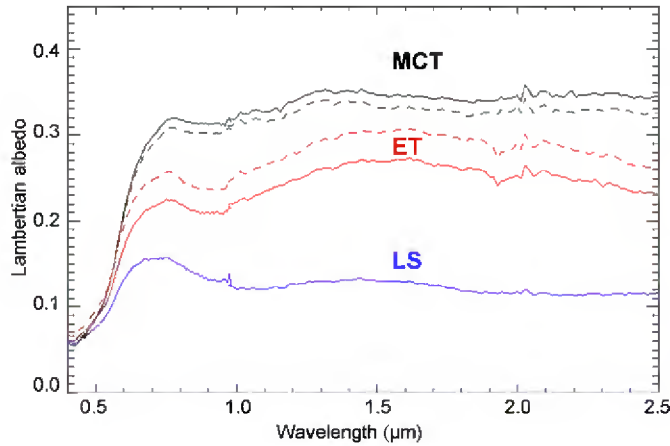


Fig. 12. Spectra shown in Fig. 8 in the 0.4–2.5 μm wavelength interval. The unique spectral characteristics of the unit E (red dashed and solid lines, ET) are the band at 1.9 μm , the strong red slope in the 1.0–1.4 μm range and a strong band around 0.9 μm . The blue spectrum LS, extracted from the landing site area, has a very flat shape in the NIR range, indicating the presence of spectrally featureless component(s). The unit MCT (black solid and dashed lines) lacks of spectral signatures, especially for wavelength larger than 0.7 μm , which is typical of the nanophase oxides (see text). Note that the stochastic S/N exceeds 200 at 1.5 μm for the spectra.

ing a pronounced NIR red slope (Fig. 18). Schwertmannite [$\text{Fe}^{3+}_6\text{O}_{16}(\text{OH})_{12}(\text{SO}_4)_2\cdot n\text{H}_2\text{O}$; Dyar et al., 2005] has a strong reddening in the 1.0–1.4 μm range and the 1.9 μm band (Bishop et al., 2005; Cloutis et al., 2006). In contrast, the Mg-, Al-, Ca-, K-bearing and Fe-free sulfates as well as the Fe^{3+} with additional cation-bearing sulfates exhibit numerous other spectral features in the 1.7–2.5 μm range that do not match the spectra of the etched terrains (Cloutis et al., 2006). There is the possibility that these bands are not detected because they are below the signal-to-noise resulting from low concentration.

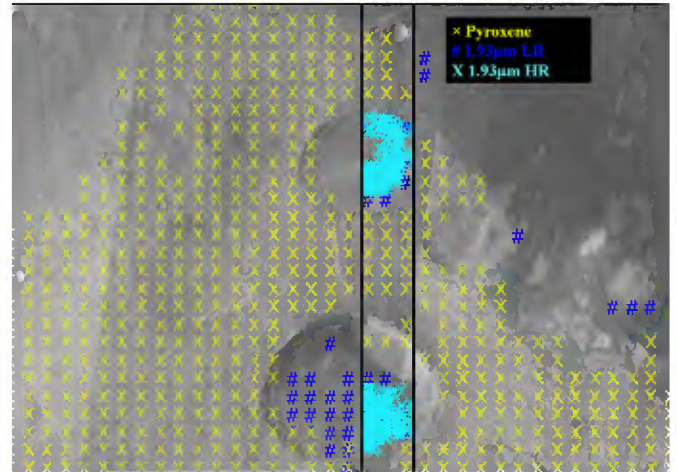


Fig. 14. Comparison between the mappings of hydrated minerals using low spatial resolution (LR) data (blue symbols) and high spatial resolution (HR) data (cyan symbols). The HR track is centered at longitude 2.9° E. The pyroxene-rich terrains are outlined by yellow crosses. The mineral distributions are overlaid on a daytime THEMIS mosaic image.

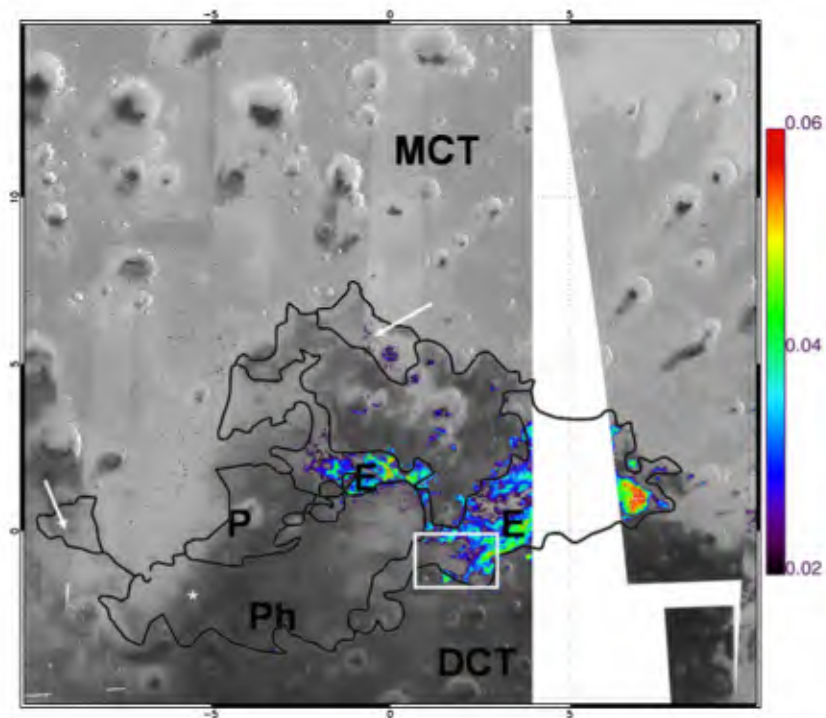


Fig. 13. Map of the 1.9 μm band depth indicator of the presence of water-bearing minerals. The white arrows show two areas of the unit E where no hydrated mineral is found. The white box indicates the region mapped in Fig. 19.

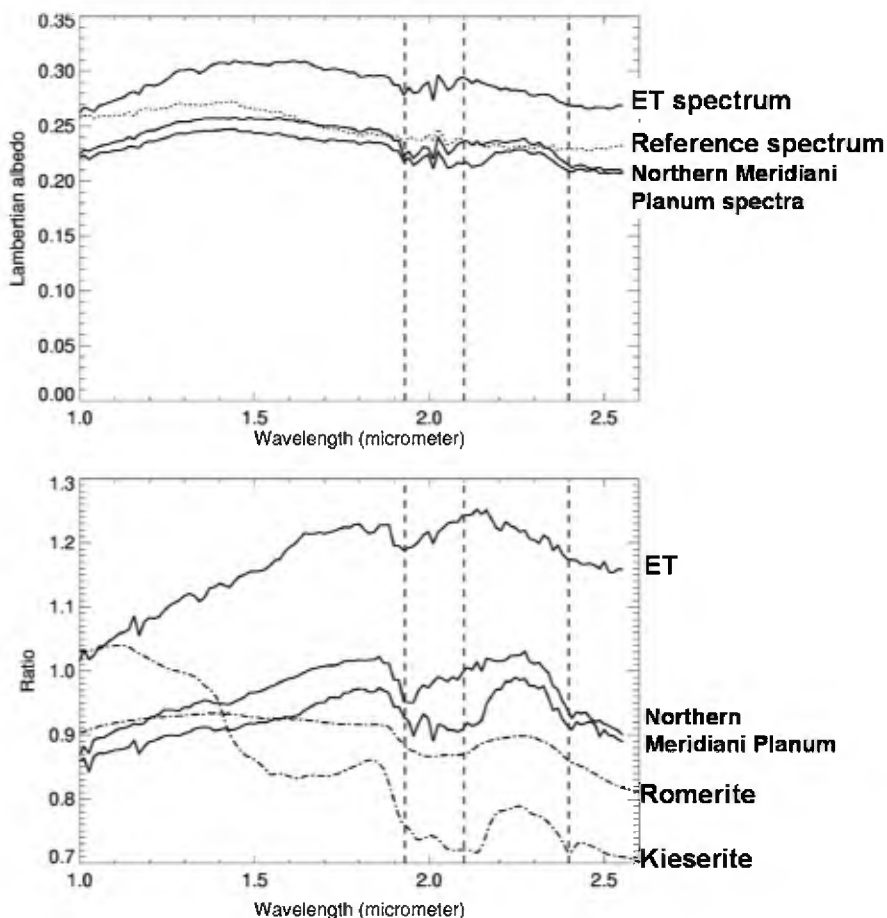


Fig. 15. Examples of spectra from the etched terrains. The instrumental error resulting from small time-dependent deviations from linearity is on the order of 1–2%. Upper: two spectra (solid lines, named northern Meridiani Planum) are extracted from the area ($\sim 2^\circ$ N, $\sim 1^\circ$ E) located in the Northern Meridiani Planum where Mg-sulfates were previously mapped by Gendrin et al. (2005), Arvidson et al. (2005) and Griffes et al. (2007). The other one (named ET spectrum, coordinates 1.7° N, 0° E) is extracted from outside this sulfate-rich region. A reference spectrum is also plotted in dotted line. Lower: the spectral ratios are compared to laboratory spectra of the mono-hydrated kieserite that exhibits a large $2.1 \mu\text{m}$ and to the polyhydrated sulfate romerite. Note that the spectral characteristics of the “ET” spectrum are not well described by the laboratory spectra of the sulfates. In particular, there is no well defined $2.4 \mu\text{m}$ band due to the $(\text{SO}_4)^{2-}$ stretch, making this spectrum similar to the spectra seen in most of the etched terrains (Fig. 18).

From synthetic spectra simulating a mixture of a hydrated mineral (gypsum) and martian dust, we investigated the detection threshold in terms of abundance with OMEGA (Poulet et al., 2007). A mixture with a gypsum concentration slightly greater than 5% (resp. 10%) can be considered as a positive detection assuming a gypsum grain size of $10 \mu\text{m}$ (resp. $5 \mu\text{m}$). The analysis was based on the $1.9 \mu\text{m}$ band, but a look of the synthetic spectra (Fig. 4 of Poulet et al., 2007) suggests that the $2.4 \mu\text{m}$ band should roughly provide similar detection threshold on the abundance. Although this type of analysis should be performed on others minerals with other spectral parameters as well in order to set a limit on the abundance, this indicates that the minerals if present are likely a minor component (assuming similar assumptions on particle size and mixture).

Spectral ratios extracted from the unit E have been also compared to different H_2O - and/or OH-bearing ferric oxyhydroxides (Fig. 18). The unit E spectral shape and $1.9 \mu\text{m}$ band are well reproduced by lepidocrocite and ferrihydrite. A mixture of these minerals can be also considered. Note however that lepidocrocite should not have a $1.9 \mu\text{m}$ band from H_2O . Presumably, the $1.9 \mu\text{m}$ results from H_2O trapped during pre-

cipitation of the mineral. Other oxyhydroxides/hydroxides such as goethite $[\text{FeOOH}]$ and gibbsite $[\text{Al}(\text{OH})_3]$ can be ruled out because these minerals do not have a $1.9 \mu\text{m}$ band due to the water molecule and/or usually present strong OH signatures not identified in the OMEGA spectra. A unique identification is however difficult because the end-members of its mineral class are numerous and spectrally similar.¹ Finally, we note that there is also an indication of a shallow $2.3 \mu\text{m}$ band in one of two martian spectra shown in Fig. 18, but the reality of this band is called into question because the band depth is at the limit of the detection threshold of 2% defined in Section 2.1.

¹ There is an ambiguity in the interpretation directly derived from a spectral comparison from laboratory measurements. The formulae of most of the hydroxides do not contain H_2O , although a strong $1.9 \mu\text{m}$ band is very often present in the laboratory spectra. This band is attributed to the combination bend plus stretch modes in water at ~ 1.91 and $\sim 1.95 \mu\text{m}$. It is uncertain if the crystal structure of some natural samples of oxyhydroxides/hydroxides really contains water molecules or if the feature comes from ambient environmental laboratory conditions and associated adsorbed and/or naturally occurring trapped water.

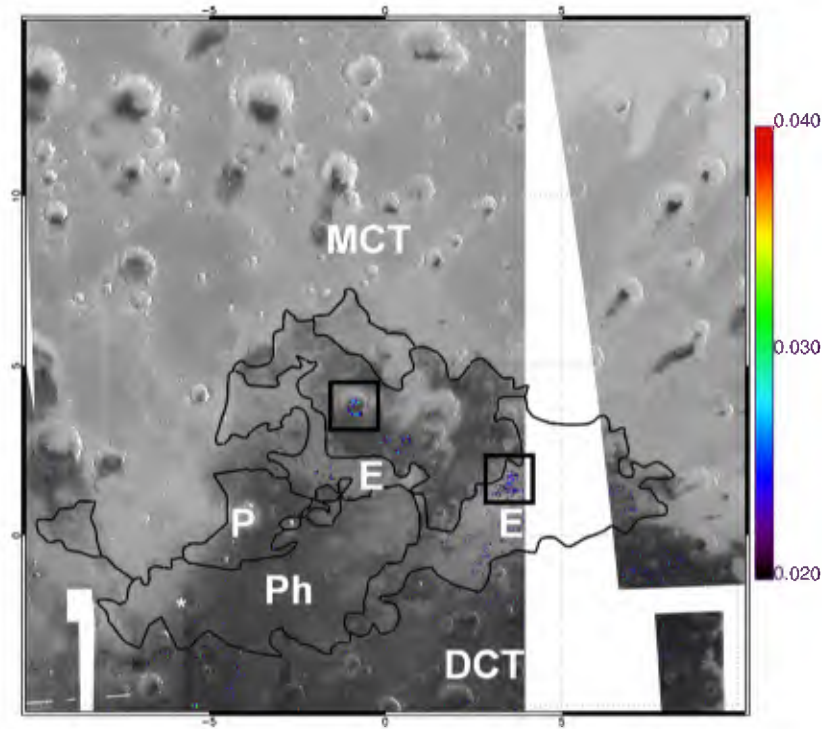


Fig. 16. Map of the 2.3 μm spectral index showing the distribution of the Fe/Mg–OH phyllosilicates. The gray scale corresponds to the albedo at 1.08 μm with a range from black (10%) to light gray (45%). The color bar gives the values of the 2.3 μm spectral index (Table 1). The two black squares show the two spots where the detections are reliable.

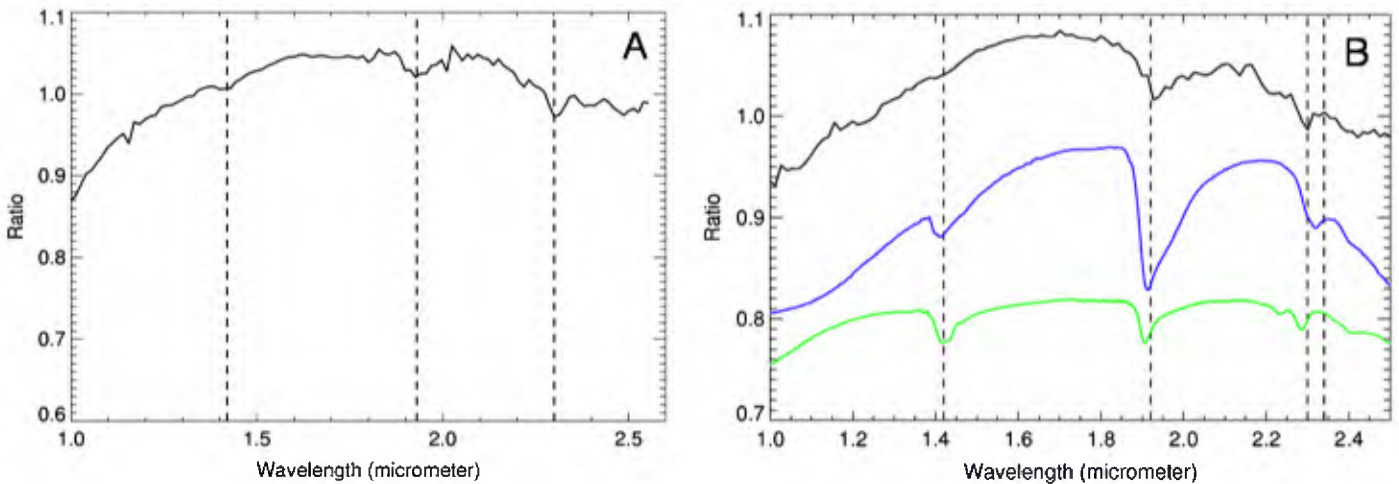


Fig. 17. Examples of a spectrum for a phyllosilicate-bearing terrain. (A) The spectrum has been extracted from the crater located at 3.65° N , 0.9° W , and ratioed to a reference spectrum of the same OMEGA cube. Absorptions at 1.4, 1.9 and 2.3 μm are characteristics of the Fe/Mg-bearing phyllosilicates. Note however that the strength of these bands are relatively smaller than those observed in the spectra extracted from the phyllosilicates-rich terrains identified on Mars (Poulet et al., 2005). Different factors such as a larger contamination by other minerals could explain the weakness of the bands. (B) Same as upper figure but the spectrum has been extracted from a terrain of the unit E located at 1.60° N , 3.55° E . The ratioed spectrum is compared to two laboratory spectra of phyllosilicates (Fe-rich smectite in green, Mg-rich saponite in blue). Absorptions at 1.4, 1.9, 2.3 and 2.35 μm are characteristics of the Fe/Mg-bearing phyllosilicates.

A major spectral feature of the etched terrains is the presence of a strong ferric signature in the 0.9–1.4 μm wavelength region (see Section 3.2 and Fig. 12). A comparison of Figs. 11 and 13 shows that the spatial distributions of the crystalline ferric feature and of the 1.9 μm band depth are rather well correlated. At the OMEGA scale, mixture of different minerals is very likely. Thus the spectral characteristics of the unit E could be explained by a mixture of poorly crystalline ferric oxides

and hydrated minerals such as sulfates whose spectral features could be masked by the ferric oxides. The physical setting of the minerals mixture could occur at small scale, possibly at microscopic scale. Moreover, the spectral features diagnostic of the sulfates can be affected even by a small amount (about 10%) of ferric oxides/or oxyhydroxides (Cloutis et al., 2006). Therefore a complex mixture of sulfates and iron oxides/oxyhydroxides in larger proportions, which could hide the spectral features at

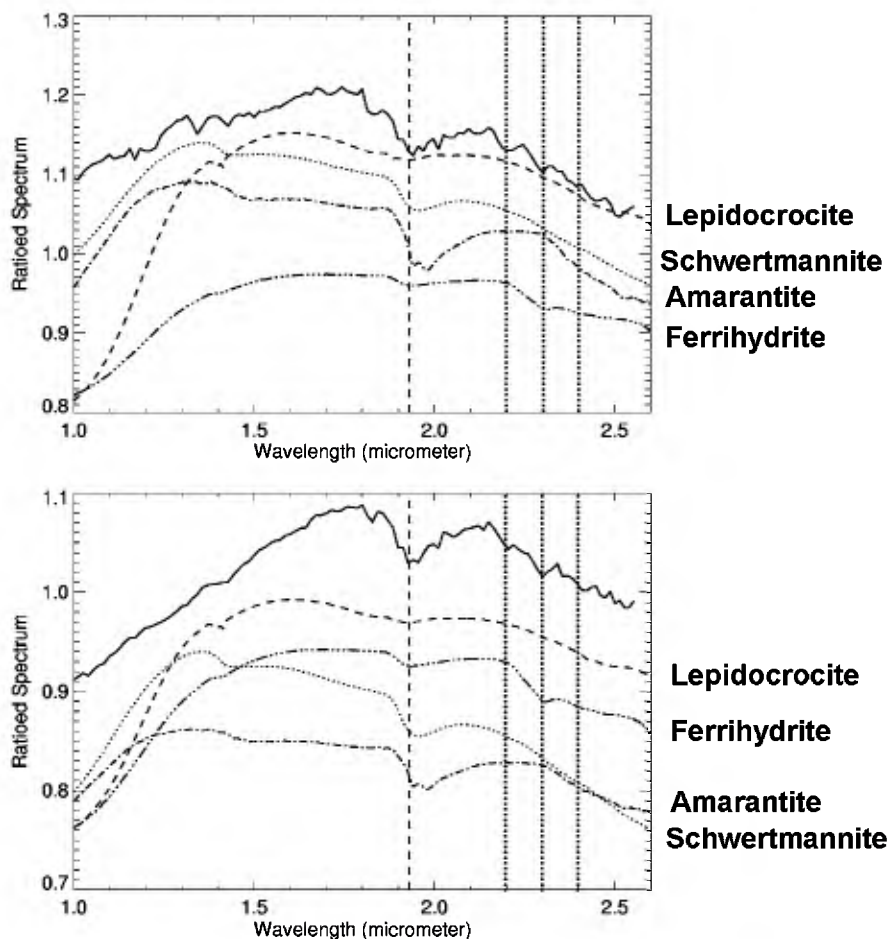


Fig. 18. Examples of spectra extracted from the unit E. The spectra (continuous lines) are ratioed to a reference taken in the same OMEGA cube. The instrumental error resulting from small time-dependent deviations from linearity is on the order of 1–2%. Upper: the spectrum is compared to the ferric sulfates amaranтите and schwertmannite, and the hydroxides ferrihydrite and lepidocrocite. The laboratory spectra provided by Brown University are scaled and shifted to facilitate the comparison with the OMEGA spectra. The lack of any spectral feature except for a 1.9 μm band is typical of the spectra of the unit E. Lower: this second ET spectrum is compared to the spectra of amaranтите, ferrihydrite and lepidocrocite. The vertical lines indicate the wavelength positions of the major absorptions of the hydrous sulfates and the phyllosilicates. Dashed line: H_2O stretching overtones; dotted line: overtones of the ν_3 S–O asymmetric bend at 2.40 μm ; solid lines: Al–OH at 2.20 μm and Fe/Mg–OH at 2.30 μm .

2.1 and 2.4 μm specific of Mg-sulfates, cannot be totally excluded.

3.3.2. Correlations with thermophysical properties

3.3.2.1. H_2O -bearing terrains In the previous section, we discussed that the 1.9 μm band depth was not uniform over the entire unit E. The region between 0° – 1.7° S and 0.6° – 3° E is an example of this variation, showing exposures of hydrated mineral-rich terrains juxtaposed to non-hydrated terrains (Fig. 19). The boundary between the units E and DCT traverses the study area, and a better understanding of the surface composition is obtained by mapping the pyroxene distribution. As expected, there is a clear correlation between unit DCT and the spatial distribution of pyroxene. A pyroxene occurrence centered at 0.5° S– 1.5° E is evident in the unit E, explaining lack of the hydrated minerals in this zone. This isolated pyroxene-rich deposit, which is located at lower altitude than the surrounding etched terrains could correspond to a window of the pyroxene-rich unit DCT. Conversely, a small deposit of hydrated minerals is seen inside the unit DCT at 1.4° S, 1.55° E. A comparison of

the mineral distributions with the predawn THEMIS thermal IR map (roughly equivalent to the thermal inertia map) indicates a good correlation between high thermal inertia areas (white areas) and hydrated terrains, and between intermediate thermal inertia (gray areas) and pyroxene-rich terrains. A third component in the THEMIS temperature map is defined by the dark areas, where the lowest temperatures are found. Because these areas also have a higher albedo (~ 0.3 at 1.5 μm), we interpreted them as dustier and less-rocky surfaces. The boundaries of the mineral distributions follow the sharp thermal contacts between the E and DCT units, with thermal inertia increasing by several hundred units over less than a few kilometers as shown by Hynek (2004). Far from this region, another correlation between band depth and thermal properties is found at the eastern part of the unit E (1° N, 7° E). This area, which has the strongest signature at 1.9 μm , has some of the highest thermal inertias of the unit E (Hynek, 2004). All these observations imply that these minerals do not correspond to mobile, surficial deposits but occur within in-place rock exposures.

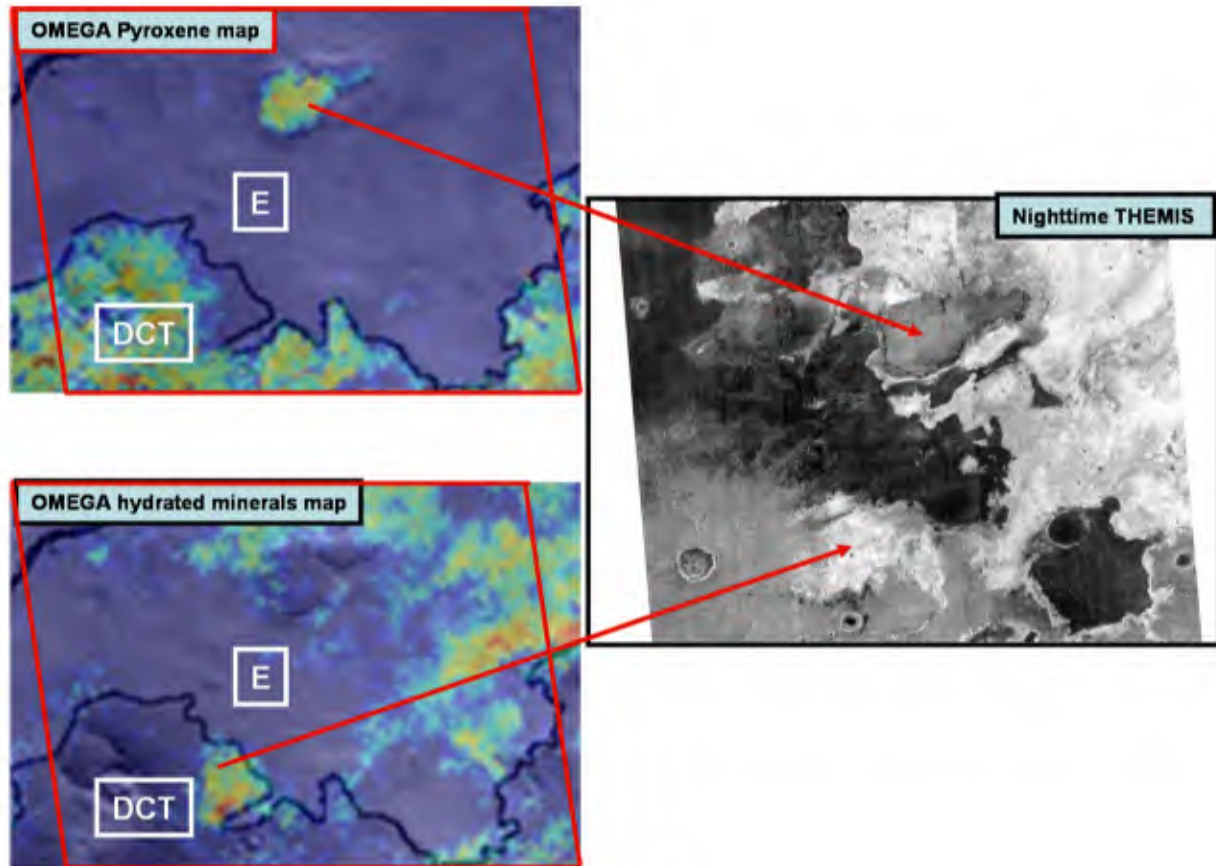


Fig. 19. Spectral diversity at the border of the unit E and the unit DCT (0° – 1.7° S, 0.6° – 3° E). The distributions of the pyroxene and the hydrated minerals are shown and compared to a nighttime THEMIS mosaic. The color scales are the same than those used for the regional mappings (Fig. 3 for the pyroxene and Fig. 13 for the hydrated minerals). The boundaries between the etched terrains (unit E) and the dissected cratered terrains (DCT) are indicated on the two mineral maps. Also shown are locations of the two compositional anomalies and their corresponding thermal properties by arrows. The presence of the hydrated minerals is strongly correlated to the terrains exhibiting warmer nighttime temperature (equivalent to larger thermal inertia).

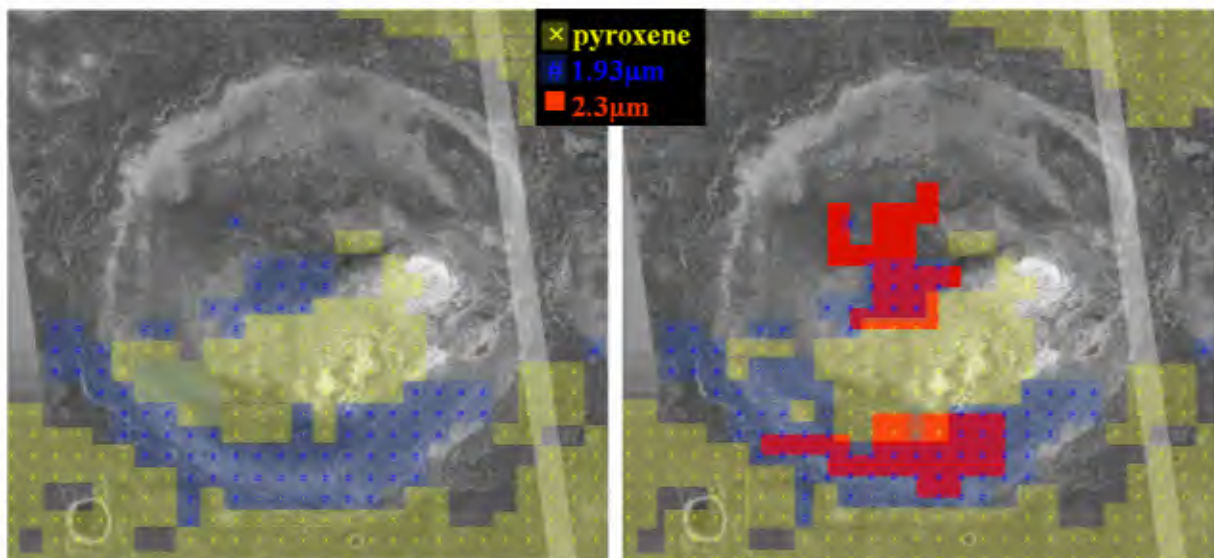


Fig. 20. Location of the phyllosilicate-bearing terrains in crater located at 3.65° N, 0.9° W. The mapping of three indexes (pyroxene in yellow, $1.9\ \mu\text{m}$ band in blue and $2.3\ \mu\text{m}$ band in red) are overlaid on a nighttime THEMIS mosaic.

3.3.2.2. Phyllosilicate-rich terrains We now focus on phyllosilicates occurrences. The deposit inside the crater centered at 3.65° N, 0.9° W is actually composed of two separated zones

(Fig. 20): one is close to the center of the crater and the second one goes from the crater floor up the southern rim. However, the geomorphology and the thermal properties of these

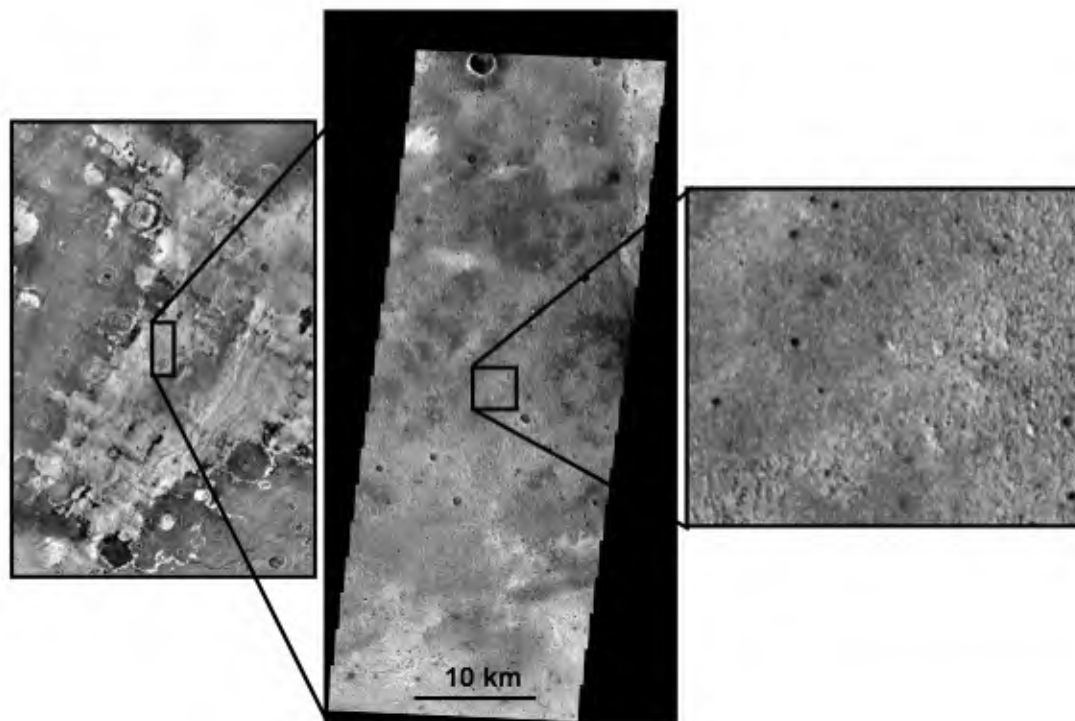


Fig. 21. Geomorphic context of the second phyllosilicate-bearing spot. Visible THEMIS V16650014 image (centered at 1.55° N and 3.52° E) and a close-up that covers the spot centered at 1.60° N, 3.55° E is shown. The location of the visible THEMIS image is presented on a context view obtained from the THEMIS-derived thermal inertia map from Hynek (2004), where the unit E corresponds to the whitish areas. No difference in terms of geomorphology and thermal inertia between the phyllosilicate-rich terrains and the surrounding etched terrains is observed.

terrains are not significantly distinct from those of the surrounding terrains. The second deposit occurs inside the unit E near 1.55° N, 3.6° E with no distinct thermal properties (Fig. 21). THEMIS visible image data as well as MOC images (for instance MOC m2101171) reveal an etched surface with no layers and disturbed only by sub km-sized craters. In contrast to other phyllosilicates-bearing terrains detected by OMEGA (Poulet et al., 2005), no geomorphologic features distinct from the rest of the unit E were detected.

4. Summary of the mineralogy and comparison with previous works

4.1. Terra Meridiani

As noted in previous sections of this paper, mineral distributions mapped from OMEGA data for the study area correlate well with geologic units and their thermophysical properties. The spectrally dominant minerals identified in the unit DCT are low-calcium and high-calcium pyroxenes and the spectra representative of the diversity of the pyroxene spectral index are well reproduced by a mixture of pyroxenes and feldspar as a neutral phase. The best picture of the surface of the unit DCT is a soil of basaltic composition with sand-sized particles (in the 10s to 100s μ m). We interpret the nature of this soil as a result of the erosion resulting from meteoritic impacts and aeolian erosion of the Noachian terrains.

The unit P is the only exception where no correlation between the surface composition and the geologic boundaries

exists. The surface composition of the center and of the eastern part is similar to the pyroxene-rich DCT unit whereas the western part is more similar to the MCT unit. We thus assign the P unit to the DCT unit. The MCT unit is covered by dust whose spectral signature is dominated by nanophase ferric oxides. Such a composition is consistent with other parts of Arabia Terra (Poulet et al., 2007). This suggests that the unit MCT has the same origin as the overall Arabia Terra deposits as discussed in more detail in Section 4.2.

The mantle MCT covers the northern part of the unit E. The exposures of the etched terrains that exhibit high thermal inertia are locations where we infer the presence of hydrated minerals. We confirm the presence of sulfates in the west-northern part based on previous work (Gendrin et al., 2005; Arvidson et al., 2005; Griffes et al., 2007). Small occurrences of phyllosilicates-rich terrains are reported, but no geomorphologic characteristics distinct from those of the surrounding terrains have been identified. Although more work has to be done on this deposit to better understand its relationship with the other etched terrains, our observations suggest that the phyllosilicates may form from the same solution and during the same period as the other etched terrains. Poorly crystalline ferric components, which are identified by a strong Fe^{3+} band in the 0.7–1.35 μ m region, cover almost the entire unit E. Ferric hydrous-oxyhydroxides, oxyhydroxides and sulfates (ferrihydrite, lepidocrocite, schwertmannite, amaranthite) are possible candidates to explain the unique spectral properties. Interestingly, a Fe^{3+} -bearing phase in addition to jarosite and hematite has been proposed to explain the Mössbauer spectra of the outcrops (Klingelhöfer et al., 2004;

Morris et al., 2006) observed by Opportunity, and could be representative of the ferric minerals detected by OMEGA. In particular, ferrihydrite, lepidocrocite, schwertmannite and superparamagnetic hematite and goethite were proposed as possibilities for the Fe^{3+} signature (Morris et al., 2006). A microscopic mixture of poorly ferric oxides with other sulfates is also proposed in this paper, but such a composition has to be investigated further by laboratory VNIR spectroscopic measurements.

The lack of any signature other than H_2O over large parts of the unit E that are not covered by basaltic soil and hematite lag is rather surprising. Jarosite, the only sulfate mineral unambiguously identified on the outcrops by the MER experiments should be easily detected in the NIR range if present in sufficient abundance. This mineral is characterized by narrow absorptions at ~ 1.47 and ~ 1.85 μm and by a 2.27 μm doublet that were not observed in the OMEGA spectra. The spectral measurements done by Cloutis et al. (2006) on a laboratory mixture of jarosite with 10% of goethite and hematite indicate that the spectral features of the jarosite mineral are still present although less pronounced. This remark raises a caveat in our analysis: the spectra of complex mixtures of materials with different mineral concentrations are not known as discussed below.

If ferric or ferrous sulfates, in addition to the possible presence of schwertmannite or amarantite are present, three effects could be proposed to explain the absence of their spectral signatures: poorly crystalline nature, complexity of the mixture, or loss of water molecules that gives rise to structural breakdown of the unit cells near the surface of the deposits. The poorly crystalline structure of the unit E material is clear as discussed in Section 3.2. It is well known from numerous spectroscopic studies that decreases in particle size of a weak absorber causes the absorptions to weaken as volume scattering plays a diminishing role relative to first surface interactions (e.g., Cooper and Mustard, 1999). The identification could be also complicated by the fact that numerous intermediate phases of poorly ordered iron oxides, oxyhydroxides, and/or oxyhydroxy-sulfates can be formed in aqueous systems depending on the OH/Fe ratio (Schwertmann et al., 1999). These phases are not well identified in the NIR. Alternatively, Hasenmueller and Bish (2005) have demonstrated that only small temperature excursions of a few tens of degrees above the ambient temperature can destroy hydrated iron sulfates and, consequently, their spectral signatures. A dehydration of the upper surface layer of the Late Noachian unit E may have also occurred under long time exposure to the present dry martian conditions. In any case, more laboratory measurements are needed to test the spectral responses of these effects.

Although the Ph unit lacks strong mineral signatures, careful analysis and comparison with other spectral units indicate the presence of olivine and a small amount of pyroxene in some areas. Moreover, one of the flattest slopes in the VNIR wavelength range seen on Mars strongly suggests the presence of coarse grains of oxide (likely spectrally featureless crystalline gray hematite as reported by Christensen et al., 2000). The comparison of the mapping of the ferric component reported in our study with the gray (specular) hematite spatial distribution generated by TES observations reveals important differences,

because the two wavelength regions are differentially affected by texture, coatings, and particle size. Thermal infrared measurements are well suited for detection of a broad range of silicate, including phases that are spectrally neutral in the NIR (e.g. feldspar). Conversely, the thermal infrared is not sensitive to poorly crystalline ferric oxides/oxyhydroxides or even well-crystalline ferric oxides/oxyhydroxides with submicrometer or smaller grain sizes, which explains the non-identification of these components over the etched terrains. Finally, hydrated sulfate minerals have not been detected from martian orbit over the landing site or over the unit Ph at levels above the detection limit defined in this study. This results from the fact that the surface fraction of the sulfate-bearing outcrops visible in the hematite-bearing plains is very small relative to the hundreds meters size of OMEGA pixels (Arvidson et al., 2006) and/or that the surface has been altered to remove the signatures relative to the rock volumes.

4.2. Western Arabia Terra

The mantle of dust that contains nanophase ferric oxides that dominates the spectra of the unit MCT in the northern Meridiani continues towards western Arabia Terra. This composition is the same as found in other martian bright regions, suggesting a similar origin. The nanophase ferric oxides on Earth are commonly produced from hydrolytic alteration, as in palagonitic tephra (e.g., Morris et al., 2000). Perhaps aqueous alteration occurred in the past and the water has been removed by aging processes resulting from a long exposure to the dry and low pressure martian atmosphere and to the UV irradiation. Alternatively, it has been proposed that the anhydrous nanophase ferric oxides correspond to a gas/surface weathering process without liquid water involved (Bibring et al., 2007). This product could likely be mobile (“dust”).

Interpretations of the Arabia Terra deposits are multiple and include eolian dust mantles (Scott and Tanaka, 1986; Moore, 1990), pyroclastic ash (Moore, 1990), paleopolar deposits (Schultz and Lutz, 1988), and subaqueous deposits (Edgett and Parker, 1997). More recently, it has been proposed that the Arabia deposits may represent relict dust and ice sediments (Tanaka, 2000). By using the Mars general circulation model (MGCM), Newman et al. (2005) provided a new view of the dust activity during martian history. Their MGCM simulations predict an accumulation of dust on the Arabia regions in the case where Mars is at high obliquities ($>35^\circ$). The origin of the mantle seems therefore to be fully consistent with an eolian dust deposition.

As noted previously in this paper numerous dark streaks in the MCT unit are enriched in pyroxene relative to surrounding bright surfaces. The low albedo deposits (dunes in most cases: Edgett, 2002) inside the craters from which the dark streaks emanate are enriched in pyroxene. This similarity in mineral composition indicates that the dark dunes directly supply sediment to create the streaks that are dark material on top of brighter material. Moreover, the decrease of the band depth from the interiors to the dark streaks can be interpreted either as a grain size effect, with the streaks consisting of grains finer

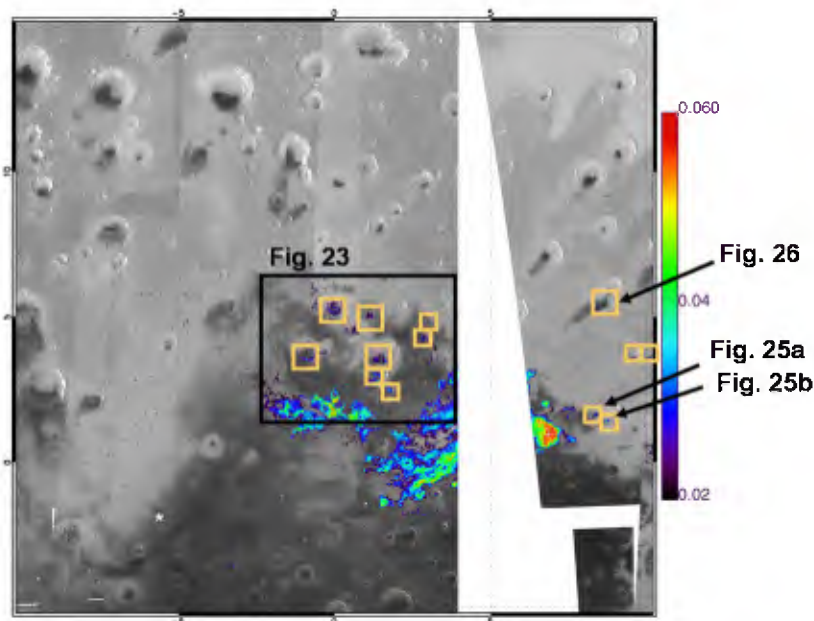


Fig. 22. Crater interiors in southwestern Arabia Terra that exhibit hydrated minerals deposits (yellow squares).

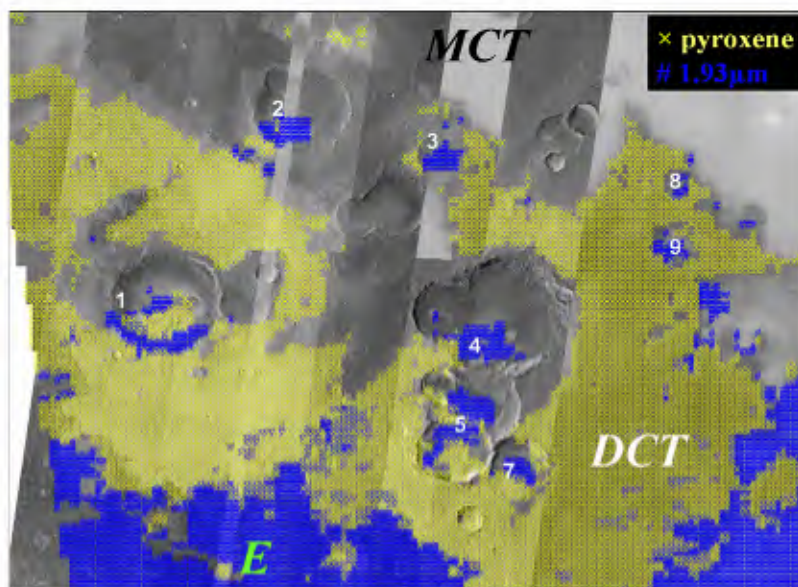


Fig. 23. OMEGA distribution of the pyroxene and hydrated minerals showing the identification of hydrated deposits in craters. Base map is a mosaic of THEMIS images. For reference, the crater are numerated.

than those that comprise the dunes and/or a decreasing relative abundance of pyroxene possibly due to a larger dust contribution.

Of special interest is the detection of hydrated terrains inside craters of Arabia Terra. Fig. 22 provides a regional view of the hydrated deposits detected inside craters. The spectral characteristics are the same than those found over most of the etched terrains: a 1.9 μm band associated with a significant red slope between 1 and 1.35 μm . In general, the hydrated deposits are spatially well separated from the pyroxene-rich regions (Fig. 23). Both the morphology and the thermophysical properties of these hydrated terrains inside craters favor a close relationship with the hydrated etched terrains of the unit E.

MOC images, where available, reveal that the hydrated deposits are strongly eroded and expose light-toned material similar to what is found in the unit E. Fig. 24 shows that these interior deposits also have higher nighttime temperatures than surrounding surfaces. Finally, the absolute elevation of the bottom of the hydrated deposits in craters is between -2000 and -1000 m, with a rough decrease from east to west in good agreement with the regional tilt.

The occurrences of layered rocks in craters or crater-like depressions in western Arabia Terra are not hydrated within detection limits or only a fraction of the deposit is hydrated. Examples are primarily in Fig. 25: the 1.9 μm band occurs only in some places in the terrains with the highest nighttime tem-

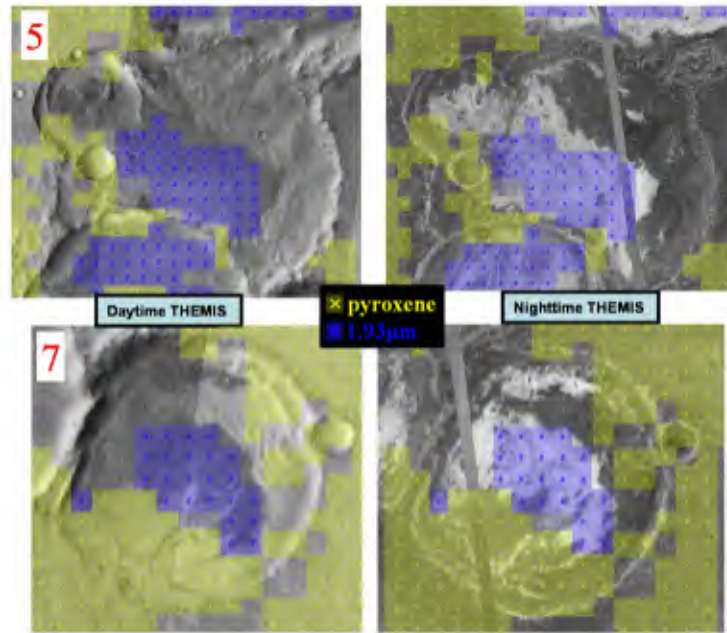


Fig. 24. Close-up of the distributions of the pyroxene and the hydrated minerals for two craters. Base maps are daytime THEMIS (left) and nighttime THEMIS (right) mosaics. There is a remarkable correlation between the distribution of the hydrated minerals (blue pixels) and the terrains with the high thermal inertia. The hydrated deposit seen in the north corresponds to the crater 4. MOC images reveal that these terrains are strongly eroded, layered and light-toned mounds (Edgett, 2002).

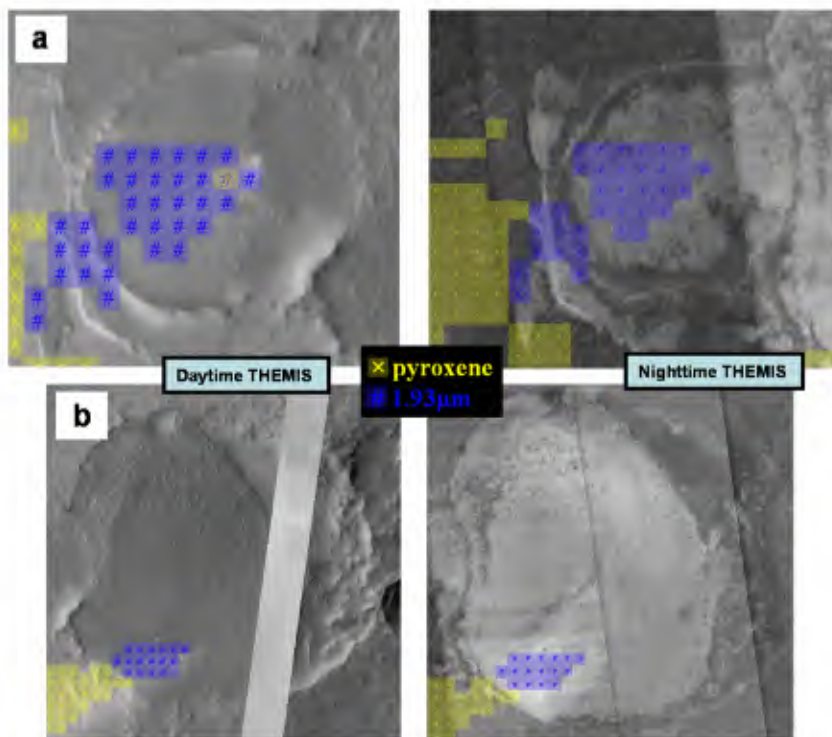


Fig. 25. Same as Fig. 24.

perature (the surrounding terrains being composed of pyroxene or dust). It has been shown that many mounds composed of layered materials within the craters in Arabia Terra exhibit a 3 μm band in OMEGA data that is significantly greater than the surrounding terrains (Milliken et al., 2005). This band is diagnostic of adsorbed water and/or hydrated phases (Jouglet et al., 2007).

The lack of diagnostic absorptions in the 1–2.5 μm range, however, makes it difficult to identify the host for the water. MOC and THEMIS images reveal that these mounds are commonly covered with dust, as confirmed by their higher albedo, which likely masks the 1.9 μm signature (the stronger 3 μm is interpreted to be less sensitive to the dust coverage).

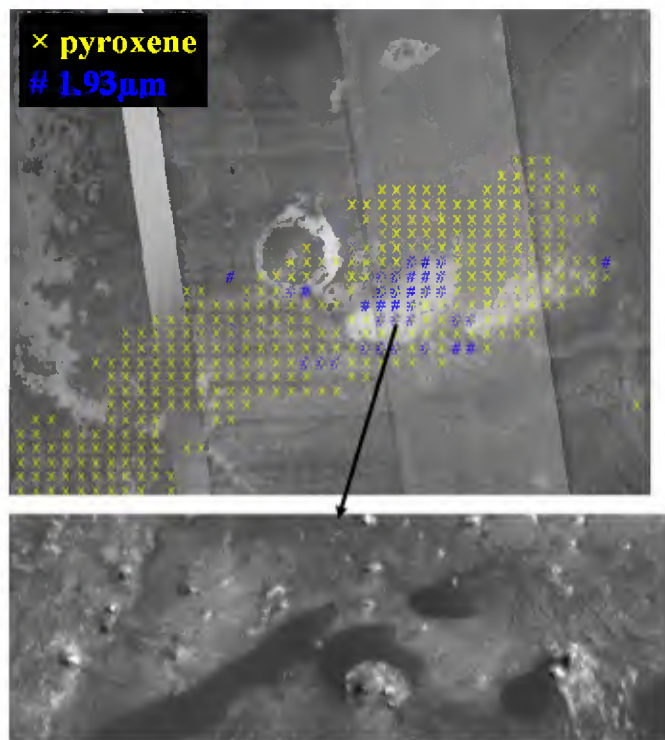


Fig. 26. Same as Fig. 23 but with a detail of an area where both pyroxene (in yellow) and hydrated minerals (in blue) are mapped. MOC image reveals a dune field that extends to the south–west where pyroxene is mapped as well as bright terrains that extend to the north where hydrated minerals have been identified (blue symbol). This suggests that the best model to explain the mixture of pyroxene and hydrated minerals is a spatial mixing, where the basaltic dunes should cover the light-toned and hydrated outcrops.

In a few cases an overlap occurs between the spatial distributions of the 1.9 μm from hydrated minerals and the 2 μm bands from ferrous silicates. The crater located at 5.4° N, 8.4° E is a typical example, where several pixels (blue pixels in Fig. 26) indicating the presence of hydrated minerals collocated with mafic materials (yellow pixels in Fig. 26). As expected, the pyroxene-rich hydrated mineral-free terrains are well correlated with dark streaks, whereas nighttime THEMIS images reveal that the hydrated minerals are distributed over terrains with higher temperatures. A subframe of MOC image M07-05541 in Fig. 25 shows the morphology in detail: dark dunes overlie a brighter etched terrain. The dark dunes from which the dark streak emanates are likely made of basaltic pyroxene-rich materials, whereas the brighter underlying etched terrains contain hydrated minerals. At the OMEGA pixel scale these two minerals are mixed so that the spectral characteristics of this region are compatible both with pyroxene and hydrated minerals.

Finally, the proximity of the dark dunes to the layered mounds in the craters of this unit suggest a connection (Edgett, 2002). However, the difference of composition between the pyroxene-rich dark dunes and the hydrated layered mounds in the craters suggests that layered terrains do not supply the dunes. Nevertheless, we cannot totally exclude the presence of pyroxene-rich layers in the layered hydrated units, which would be too small to show up spectrally in $\sim 500\text{--}3500$ m/pixel

OMEGA data. Over time, these layers may erode into sand-sized particles to form the dunes.

Higher spatial resolution data are required to test this possibility.

5. Implications for the formation of the etched terrains

This section presents the consequences of our inferred mineralogical composition of the etched terrains on their formation. The discussion assumes that what we see from OMEGA is representative of the volume of unit E. To date, three formation scenarios have been proposed to explain the various features of the deposits in Terra Meridiani: the sedimentary/evaporite scenario (Squyres et al., 2004), the surge deposits formed by a series of large impact (Knauth et al., 2005) and volcanic scenario (McCullom and Hynek, 2005). We now make the case that none of these models can satisfactorily explain the mineralogy inferred by our observations.

5.1. Can the formation models of the Meridiani Planum outcrops be applied to the entire etched terrains?

5.1.1. Comparison between the OMEGA mineralogy and the alternative formation processes

The apparent absence of phyllosilicate deposits over Meridiani Planum has been advanced by Knauth et al. (2005) to refute the formation of sulfate-rich outcrops by alteration of siliclastic material by acid groundwaters. Alternatively, the same authors propose a formation by impact surge. However, our phyllosilicate detections, although tenuous and localized, are not in good agreement with the prediction of the impact surge scenario.

The mineralogy derived from the OMEGA observations also has implications regarding the formation of the outcrops as proposed by McCullom and Hynek (2005). Their model mineral assemblage includes components of quartz, alunite and diasporite. Although the quartz is spectrally neutral in the NIR range and could be an end-member not identified by OMEGA, alunite and diasporite would have been definitively identified in the etched terrains by very strong features at 1.4, 1.78, 2.2, 2.5 μm . Thus we do not see the assemblage of minerals predicted in their 2005 paper. However, this derived assemblage was one run of many and is not necessarily the final mineral assemblage at Meridiani (B.M. Hynek, personal communication). During acid-sulfate alteration of the ash, the original igneous minerals could be replaced by alteration products including phyllosilicates (e.g., nontronite, saponite), amorphous silica, hematite and sulfate salts (McCord and Hynek, 2007). These minerals are thus more compatible with the diverse mineralogy observed in the etched terrains. On the other hand, the fact that the ferric sulfates are not the dominant components of the resultant mineralogy appears to be inconsistent with our preferred mineralogy for most of the etched terrains. Other aspects of the volcanic scenario remain to be explained (Squyres et al., 2006).

Finally, the methodology that consists to compare a mineralogy derived from remote sensing observations against theoretical equilibrium models has limitations, because the mineral

assemblage may be controlled by kinetic and not equilibrium processes. Therefore, it appears to be premature to totally discount the possibility of a volcanic (or impact) origin of the Meridiani deposits on the basis of mineralogy, and further investigation of theoretical equilibrium models should be pursued.

5.1.2. Comparison between the OMEGA mineralogy and the MER team formation process

A viable model for the formation of the outcrops at Meridiani Planum is a “dirty evaporite,” i.e. an aqueous alteration of olivine-rich basaltic materials under acidic, oxidizing and arid conditions (Squyres et al., 2004; Tosca et al., 2005). The modern Meridiani plains later formed via wind erosion of sedimentary outcrops and accumulation of a thin aeolian deposit of olivine-bearing basaltic sand (Klingelhöfer et al., 2004; Arvidson et al., 2006; Morris et al., 2006). The possible occurrence of olivine and pyroxene in some areas of the unit Ph is therefore in good agreement with the analysis of Opportunity’s measurements. More surprising is the absence of basaltic deposits over the rest of the etched terrains. These regions could correspond to areas where basaltic sand has been swept away by wind. Alternatively, this could be result of a stronger alteration that transformed most of the siliclastic materials. Where exposed by wind erosion to the north of the hematite-bearing plains, the ~1 km of stratigraphic section has spectrally varying signatures, including minor phyllosilicate occurrences, hydrated sulfate occurrences, hydrated ferric oxides/oxyhydroxides over most of the etched terrains, and in some locations ferric oxides. This variety suggests that the upper section examined by Opportunity may not be representative of the ~1 km in thickness of etched terrain strata.

Analyses of OMEGA data presented in this paper show that the near-infrared spectral properties of the unit E are best reproduced by ferric sulfates or ferric hydroxides, or a mixture of both. The formation of ferric oxides/oxyhydroxides and sulfates including ferrihydrite, schwertmannite and jarosite occurs under specific, but partly overlapping, pH ranges (Bigham et al., 1994, 1996; King and McSween, 2005). Sulfates and iron oxides precipitated from acidic waters commonly include the ferric mineral schwertmannite (Bigham et al., 1994, 1996; King and McSween, 2005; Fernandez-Remolar et al., 2004). To first order, the mineralogy inferred by OMEGA is therefore consistent with the outcrop mineralogy detected by Opportunity and would indicate long term low-pH environment. However, the fact that no jarosite has been detected by OMEGA in the etched terrains suggests that the solution may have a higher pH as discussed below. The analysis of natural terrestrial deposits by Bigham et al. (1996) showed that the solutions of pH between 4.5 and 6.5 produced mixture of schwertmannite and ferrihydrite. By contrast, jarosite was formed from one solution with a pH lower than 2.6. The stability of the jarosite–ferrihydrite and schwertmannite–ferrihydrite boundary both depend on $\text{Log}[\text{SO}_4^{2-}]$ and pH. A compilation of thermodynamic calculations done by King and McSween (2005) indicates that jarosite is stable on Mars at $\text{pH} < 4.6$, while schwertmannite can be stable for pH up to 7, in good agree-

ment with terrestrial samples. Another argument to support that the neutralization of the solutions that formed the etched terrains could have occurred at least locally is the presence of phyllosilicates in the unit E (Section 3.3.2). Bullock and Moore (2004) note that low acidity within a basaltic substrate cannot be sustained because of rapid reactions of the basalt with acid, leading to neutral to alkaline conditions. Thermodynamic calculations indicate that Fe-rich smectite nontronite can precipitate for pH of about 4 or larger in the case of high silica activity (Chevrier et al., 2007). Finally, the rover-based observations of the coexistence of jarosite and a Fe^{3+} -bearing phase and the near-constant elemental composition at Meridiani Planum require a model with high acidity and a low water-to-rock ratio, that is, a system that is essentially closed except with respect to volatile components (e.g., the acid-fog model or leaching model in the absence of increasing pH; Golden et al., 2005; King and McSween, 2005). The evidence for less acidic conditions as outlined above is thus more consistent with the leaching model involving higher water to rock ratios and higher pH.

Other minerals are predicted in more neutral solutions (King et al., 2004; King and McSween, 2005): Ca–Mg–Na sulfates and Ca-bearing phosphates. The presence of Mg-sulfates and polyhydrated sulfates in the northeast of Terra Meridiani is also in better agreement with the leaching model than with the more acidic fog model. Griffes et al. (2007) demonstrate that these sulfates-rich deposits are located in depressions and are at the bottom of the stratigraphic column of unit E. On Earth, the most soluble salts are formed in residual brine pools in the lowest areas (Knauth et al., 2005). Therefore, the precipitation of the most soluble sulfates such as Mg-sulfates could have been facilitated relative to topographically higher and sulfate-free terrains. The mineralogical diversity of the unit E suggests that the regional groundwater chemistry could have varied with time, becoming more acidic with time to produce local deposits of jarosite at the top of the section.

Another significant control on the chemistry of weathering solutions and resulting mineral assemblages is the bulk composition of the pristine rocks. The lack of OMEGA-observable Ca–Mg–Na bearing sulfates in most of the outcrops suggests that these phases never formed or that they were dissolved. Tosca et al. (2005) showed that the Mg-sulfates and ferrous-sulfates can be dissolved during diagenesis (three fluid flushing events). Alternatively, if the pristine rocks were enriched in Fe relative to the other elements, typical sequences of Fe-sulfate mineral formation can be occurred. For example, in areas on Earth affected by acid mine drainage, Fe^{2+} -bearing sulfates are observed close to the pyrite deposits, then a sequence is observed that begins with transition to a mixture of $\text{Fe}^{2+}/\text{Fe}^{3+}$ -sulfates, then Fe^{3+} -sulfates, and finally Fe^{3+} -oxides and oxyhydroxides (Burns, 1987). The mine drainage analogy may have limitations because terrestrial occurrences are not hosted in basaltic compositions.

The observations of strong ferric features in the entire unit E imply that the iron present in outcrop minerals is ferric; this is consistent with the conclusions based on the Opportunity results have been derived (King and McSween, 2005; Squyres and Knoll, 2005) and directly measured by the MER

Mössbauer spectrometer (Klingelhöfer et al., 2004; Morris et al., 2006): oxidizing conditions were likely during the end of their alteration. Moreover, the poorly crystalline structure of the ferric phases indicates slow growth kinetics at low temperature (Tosca et al., 2005).

5.2. Origin of the hydrated deposits inside craters of Arabia Terra

The hydrated mineral deposits found in the craters of the North of Terra Meridiani could have been emplaced in the depressions via eolian processes. However, the strong similarities between the deposits and the etched terrains in term of composition and thermophysical properties suggest that they share a common origin via aqueous processes. Because of their layered structure, a common and lacustrine origin was proposed (Malin and Edgett, 2000). The absolute elevation of the bottom of these layered units follows the regional tilt (Section 4.2). Their deposition could happen before the regional tilting. Alternatively, if they formed during the same period as the etched terrains, their formation dated after the tilting, because there is obvious morphologic evidence that the etched terrains were formed after the tilting: they cover extensive channel systems running from the cratered highlands in the southeast to highly eroded cratered terrains to the northwest (Hynek and Phillips, 2001). The detection of these hydrated mineral deposits could therefore indicate that the water-related processes in the study area occurred at an even larger scale than previously suggested by Hynek (2004). After the formation of this extensive area throughout Meridiani, extensive erosion may have occurred, leaving protected deposits inside craters.

5.3. Origins of the etched terrains

As speculated years ago by Burns (1987, 1988), the existence of ferric sulfates associated with hydroxides implies that unique conditions occurred in this region. The essential attributes of the hydrated etched terrains that must be explained by any depositional model are: a very large sedimentary deposit (~1 km thickness, several hundred thousand square kilometers based on partially eroded layered deposits observed beyond the Opportunity landing site), mineralogy of the low-pH sulfate deposit of Meridiani Planum, mineralogy of the more neutral materials constituting most of the unit E, the “dirty evaporite” sandstone nature of the Meridiani outcrops examined by Opportunity that could be likely generalized to the entire etched terrains given their similar thermophysical properties. On Earth, the ferric sulfates can have several origins: (1) oxidative weathering and dissolution of iron sulfide-bearing rocks to produce oxidizing and acidic aqueous solutions (Burns, 1987; Burns and Fisher, 1990); (2) sulfuric acid alteration of basalts by solutions associated with SO₂-rich volcanic gases in volcanic settings (e.g., Morris et al., 1996, 2000); (3) acid-fog weathering of basaltic materials (Banin et al., 1997; Tosca et al., 2004); (4) evaporation of acidic solutions (Clark and van Hart, 1981). Because the study area does not resemble to a volcanic caldera in size and shape, the origin (2) is unlikely, unless the

whole area has been stripped, possibly removing the evidence of volcanism. As discussed previously, the acid-fog weathering (origin 3) cannot well describe the more neutral environment inferred from the OMEGA observations. Several arguments, especially regarding the size of the deposits, have been pointed out to refute the evaporite origin (Knauth et al., 2005). However, sedimentary processes involving lacustrine evaporites through acidic groundwater could have formed enough sulfate-rich sand to cover a large area (Grotzinger et al., 2005; Arvidson et al., 2006). A terrestrial example, playas at White Sands, New Mexico, has been cited as an excellent stratigraphic analogue, although the mineralogical composition (gypsum-rich dunes) is different of the mineralogy of the unit E derived by OMEGA, the geographic area is much smaller than the unit E.

Among the best terrestrial analogues for explaining the mineralogy and the extent of the unit E are acid sulfate systems commonly associated with sulfide-bearing rock oxidation (origin 1). The Rio Tinto system provides a good analog where evaporation of the river water and groundwater drives precipitation of copiapite, coquimbite, jarosite, schwertmannite, and hydroxides and a depletion of siliclastic materials. Using the Rio Tinto analogy for the Burns formation proposed by Zolotov and Shock (2005), the etched terrains could have precipitated from acidic and oxidizing solutions formed from groundwater passed through iron sulfide deposits. In this scenario, it is assumed that successive rises of groundwater table occurred as proposed by Arvidson et al. (2006), and that the sulfur, iron and other species forming the unit E would come from sulfide-rich rocks associated with hydrothermal and magmatic ore deposits rather than extensive volcanism from Tharsis (and other) volcanoes. In this model, unit E would be fundamentally different from the Meridiani outcrop, which has a basaltic chemical composition when its bulk chemical composition is calculated to a sulfur-free basis.

A sequence for the formation of these Mg-sulfates and polyhydrated sulfates detected in northern Meridiani Planum from sulfide deposits could have been leaching of sulfides and transport to the surface for formation of evaporites. However, the Mg-sulfates and polyhydrated sulfates cannot be major products of this mode of formation. Indeed, Rio Tinto that is presented as a good analogue as described above does not show Mg-sulfates except for magnesiocopiapite. Consequently, a more likely formation scenario for these sulfates is that they are the results of evaporitic settings derived from acidic weathering fluids from martian basalt typically rich in Mg, Ca, Fe and SiO₂. This leads us to suggest that there are several modes for formation of etched terrains.

6. Conclusions

The mineralogy of one of the key regions on Mars has been constrained thanks to OMEGA observations, and the comparison of our results with previous studies based on orbital and ground data have lead to new or expanded insights into the nature of this region. A remarkable correlation has been found between the surface composition and the geomorpho-

logic and thermophysical properties that were used for mapping the geological units in previous works. The Noachian dissected cratered terrains are covered by basaltic sands. Nonlinear unmixing modeling shows that this unit is significantly enriched in both low-calcium and high-calcium pyroxenes (20–30% each), in agreement with the composition found in other Noachian terrains from other studies. The relative proportion of ferric-dominated and ferrous-dominated phase assemblages has been studied through different spectral parameters. The nanophase ferric oxides best explain the spectral characteristics of the mantle that covers the western Arabia Terra and the northern part of Terra Meridiani. Among the best spectral analogues of the etched terrains are Fe³⁺-bearing sulfates, oxyhydroxides or a mixture of both. The presence of a poorly crystalline ferric component has been also identified supporting oxidizing conditions during their formation. The dark streaks of western Arabia Terra originate from pyroxene-rich deposits (identified as dunes by high resolution imagery) on the crater floors, and consist of pyroxene-bearing grains finer than those of the interior deposits. The identification of numerous hydrated deposits in the craters of the northern Terra Meridiani is reported. The difference in composition between the low-albedo pyroxene-bearing dunes and the adjacent light-toned water-bearing layered deposits indicates that there is no connection between these two geological materials inside the craters.

The mineralogy deduced from the analysis of the MER-B experiment indicates that the rover studied a specific zone where the acidic conditions have been preserved, best explained by acid sulfate alteration at low water-to-rock ratios. Based on the OMEGA observations, there are several indications that the solutions from which most of the etched terrains were formed had a greater pH. The more neutral conditions are therefore more consistent with the leaching model than with the low pH acid fog model. To explain the lack of observable Mg–Ca-bearing sulfates, the lack of siliclastic residual plains and the presence of the Fe-bearing minerals under the form of ferric sulfate complexes associated with hydroxides over most of the etched terrains, we consider that the oxidative weathering of iron sulfide-bearing rocks is a possible candidate process for the formation of the minerals of the outcrops.

Acknowledgments

We acknowledge the two reviewers (B.M. Hynek and an anonymous reviewer) who provide very helpful comments. This work has been funded by the French space agency CNES and Université Paris-Sud, France.

References

- Arvidson, R.E., Seelos, F.P., Deal, K.S., Koeppen, W.C., Snider, N.O., Kieniewicz, J.M., Hynek, B.M., Mellon, M.T., Garvin, J.B., 2003. Mantled and exhumed terrains in Terra Meridiani, Mars. *J. Geophys. Res.* 108, doi:10.1029/2002JE001982.
- Arvidson, R.E., Poulet, F., Bibring, J.-P., Wolff, M., Gendrin, A., Morris, R.V., Freeman, J.J., Langevin, Y., Mangold, N., Bellucci, G., 2005. Spectral reflectance and morphologic correlations in eastern Terra Meridiani, Mars. *Science* 307, 1591–1594.
- Arvidson, R.E., and 24 colleagues, 2006. Nature and origin of the hematite-bearing plains of Terra Meridiani based on analyses of orbital and Mars Exploration Rover data sets. *J. Geophys. Res.* 111, doi:10.1029/2006JE002728.
- Bandfield, J.L., 2002. Global mineral distributions on Mars. *J. Geophys. Res.* 107 (E6), doi:10.1029/2001JE001510.
- Banin, A., Han, F.X., Kan, I., Cicelsky, A., 1997. Acidic volatiles and the Mars soil. *J. Geophys. Res.* 102, 13341–13356.
- Bellucci, G., Altieri, F., Bibring, J.-P., Bonello, G., Langevin, Y., Gondet, B., Poulet, F., 2006. OMEGA/Mars Express: Visual channel performances and data reduction techniques. *Planet. Space Sci.* 54, 675–684.
- Bibring, J.-P., and 13 colleagues, 2004. OMEGA: Observatoire pour le Minéralogie, l'Eau, les Glaces et l'Activité. *ESA Spec. Publ.* 1240, 37–49.
- Bibring, J.P., Langevin, Y., Gendrin, A., Gondet, B., Poulet, F., Berthe, M., Soufflot, A., Arvidson, R., Mangold, N., Mustard, J., Drossart, P., and OMEGA team, 2005. Mars surface diversity as revealed by the OMEGA/Mars Express observations. *Science* 307, 1576–1581.
- Bibring, J.P., and 11 colleagues, 2007. Coupled ferric oxides and sulfates on the martian surface. *Science* 317 (5842), 1206–1210.
- Bigham, J.M., Carlson, L., Murad, E., 1994. Schwertmannite, a new iron oxyhydroxysulfate from Pyhäsalmi, Finland, and other localities. *Miner. Mag.* 58, 641–648.
- Bigham, J.M., Schwertmann, U., Traina, S.J., Winland, R.L., Wolf, M., 1996. Schwertmannite and the chemical modeling of iron in acid sulfate waters. *Geochim. Cosmochim. Acta* 60, 2111–2121.
- Bishop, J.L., Pieters, C.M., Burns, R.G., Edwards, J.O., Mancinelli, R.L., Froeschl, H., 1995. Reflectance spectroscopy of ferric sulfate-bearing montmorillonites as Mars soil analog materials. *Icarus* 117, 101–119.
- Bishop, J.L., Murad, E., Dyar, M.D., 2002. The influence of octahedral and tetrahedral cation substitution on the structure of smectites and serpentines as observed through infrared spectroscopy. *Clay Mineral.* 37, 617–628.
- Bishop, J.L., Dyar, M.D., Lane, M.D., Banfield, J.F., 2005. Spectral identification of hydrated sulfates on Mars and comparison with acidic environments on Earth. *Int. J. Astrobiol.* 3, 275–285.
- Bullock, M.A., Moore, J.M., 2004. Aqueous alteration of Mars-analog rocks under an acidic atmosphere. *Geophys. Res. Lett.* 31 (14), doi:10.1029/2004GL019980.
- Burns, R.G., 1987. Ferric sulfates on Mars. *Proc. Lunar Sci. Conf.* 17 (2), *J. Geophys. Res.* 92, E570–E574.
- Burns, R.G., 1988. Gossans on Mars. *Proc. Lunar Sci. Conf.* 18, 713–721.
- Burns, R.G., Fisher, D.S., 1990. Iron–sulfur mineralogy of Mars: Magmatic evolution and chemical weathering products. *J. Geophys. Res.* 95, 14415–14421.
- Clark, B.C., van Hart, D.C., 1981. The salts of Mars. *Icarus* 45, 370–378.
- Clark, R.N., King, T.V.V., Klejwa, M., Swayze, G.A., 1990. High spectral resolution reflectance spectroscopy of minerals. *J. Geophys. Res.* 95, 12653–12680.
- Cloutis, E.A., and 11 colleagues, 2006. Detection and discrimination of sulfate minerals using reflectance spectroscopy. *Icarus* 184, 121–157.
- Chapman, M.G., Tanaka, K.L., 2002. Related magma–ice interactions: Possible origins of chasmata, chaos and surface materials in Xanthe, Margaritifer, and Meridiani Terrae, Mars. *Icarus* 155, 324–339.
- Chevrier, V., Poulet, F., Bibring, J.-P., 2007. Early geochemical environment of Mars as determined from thermodynamics of phyllosilicates. *Nature* 448, 60–63.
- Christensen, P.R., and 16 colleagues, 2000. Detection of crystalline hematite mineralization on Mars by the Thermal Emission Spectrometer: Evidence for near-surface water. *J. Geophys. Res.* 105, 9623–9642.
- Christensen, P.R., Morris, R.V., Lane, M.D., Bandfield, J.L., Malin, M.C., 2001. Martian hematite mineral deposits: Remnants of water-driven processes on early Mars. *J. Geophys. Res.* 106, 23873–23885.
- Christensen, P.R., and 26 colleagues, 2004. Mineralogy at Meridiani Planum from the Mini-TES Experiment on the Opportunity Rover. *Science* 306 (5702), 1733–1739.
- Christensen, P.R., and 13 colleagues, 2005. Mars Exploration Rover candidate landing sites as viewed by THEMIS. *Icarus* 176 (1), 12–43.
- Cooper, C.D., Mustard, J.F., 1999. Effects of very fine particle size on reflectance spectra of smectite and palagonitic soil. *Icarus* 142, 557–570.

- Dyar, M.D., Lane, M.D., Bishop, J.L., O'Connor, V., Cloutis, E.A., Hiroi, T., 2005. Integrated spectroscopic studies of hydrous sulfate minerals. *Lunar Planet. Sci.* 6. Abstract 1622.
- Edgett, K.S., 2002. Low-albedo surfaces and eolian sediment: Mars Orbiter Camera views of western Arabia Terra craters and wind streaks. *J. Geophys. Res.* 107, doi:10.1029/2001JE001587.
- Edgett, K.S., Malin, M.C., 2002. Martian sedimentary rock stratigraphy: Outcrops and interbedded craters of northwest Sinus Meridiani and southwest Arabia Terra. *Geophys. Res. Lett.* 29, doi:10.1029/2002GL016515.
- Edgett, K.S., Parker, T.J., 1997. Water on early Mars: Possible subaqueous sedimentary deposits covering ancient cratered terrain in western Arabia and Sinus Meridiani. *Geophys. Res. Lett.* 24, 2897–2900.
- Fernandez-Remolar, D., Gomez-Elvira, J., Gomez, F., Sebastian, E., Martiin, J., Manfredi, J.A., Torres, J., Gonzalez Kesler, C., Amils, R., 2004. The Tinto River, an extreme acidic environment under control of iron, as an analog of the Terra Meridiani hematite site of Mars. *Planet. Space Sci.* 52, 239–248.
- Gendrin, A., Mangold, N., Bibring, J.P., Langevin, Y., Gondet, B., Poulet, F., Bonello, G., Quantin, C., Mustard, J., Arvidson, R., LeMouelic, S., 2005. Sulfates in martian layered terrains: The OMEGA/Mars Express view. *Science* 307, 1587–1591.
- Golden, D.C., Ming, D.W., Morris, R.V., Mertzman, S.A., 2005. Laboratory-simulated acid-sulfate weathering of basaltic materials: Implications for formation of sulfates at Meridiani Planum and Gusev crater, Mars. *J. Geophys. Res.* 110, doi:10.1029/2005JE002451.
- Griffes, J.L., Arvidson, R.E., Poulet, F., Gendrin, A., 2007. Geologic and spectral mapping of etched terrain deposits in northern Meridiani Planum. *J. Geophys. Res.* 112 (E8), doi:10.1029/2006JE002811. E08S09.
- Grotzinger, J.P., and 19 colleagues, 2005. Stratigraphy and sedimentology of a dry to wet eolian depositional system, Burns formation, Meridiani Planum, Mars. *Earth Planet. Sci. Lett.* 240 (1), 11–72.
- Hasenmueller, E.A., Bish, D.L., 2005. The hydration and dehydration of hydrous ferric iron sulfates. *Lunar Planet. Sci.* 36. Abstract 1164 [CD-ROM].
- Hynek, B.M., 2004. Implications for hydrologic processes on Mars from extensive bedrock outcrops throughout Terra Meridiani. *Nature* 431 (7005), 156–159.
- Hynek, B.M., Phillips, R.J., 2001. Evidence for extensive denudation of the martian highlands. *Geology* 29, 407–410.
- Hynek, B.M., Arvidson, R.E., Phillips, R.J., 2002. Geologic setting and origin of Terra Meridiani hematite deposit on Mars. *J. Geophys. Res.* 107, doi:10.1029/2002JE001891.
- Joulet, D., Poulet, F., Milliken, R.E., Mustard, J.F., Bibring, J.-P., Langevin, Y., Gondet, B., and OMEGA team, 2007. Hydration state of the martian surface as seen by Mars Express OMEGA. I. Analysis of 3 μm hydration feature. *J. Geophys. Res.* 112 (E8), doi:10.1029/2006JE002846. E08S06.
- King, P.L., McSween, H.Y., 2005. Effects of H_2O , pH, and oxidation state on the stability of Fe minerals on Mars. *J. Geophys. Res.* 110 (E12), doi:10.1029/2005JE002482.
- King, P.L., Lescinsky, D.T., Nesbitt, H.W., 2004. The composition and evolution of primordial solutions on Mars, with application to other planetary bodies. *Geochim. Cosmochim. Acta* 68 (23), 4993–5008.
- Klinghöfer, G., Morris, R.V., Berhradt, B., Schröder, C., Rodionov, D., de Souza, P.A.J., Yen, A.S., Gellert, R., Evlanov, E.N., Zubkov, B., Foh, J., Bonnes, U., Kankleit, E., Gütlich, P., Ming, D.W., Renz, F., Wdowiak, T.J., Squyres, S.W., Arvidson, R.E., 2004. Jarosite and hematite at Meridiani Planum from Opportunity's Mössbauer spectrometer. *Science* 306, 1740–1745.
- Knauth, L.P., Burt, D.M., Wohletz, K.H., 2005. Impact origin of sediments at the Opportunity landing site on Mars. *Nature* 438 (7071), 1123–1128.
- Lane, M.D., Morris, R.V., Mertzman, S.A., Christensen, P.R., 2002. Evidence for platy hematite grains in Sinus Meridiani. *Mars. J. Geophys. Res.* 107, doi:10.1029/2001JE001832.
- Langevin, Y., Bibring, J.-P., Montmessin, F., Forget, F., Vincendon, M., Douté, S., Poulet, F., Gondet, B., 2007. Observations of the south seasonal cap of Mars during recession in 2004–2006 by the OMEGA visible/near-infrared imaging spectrometer on board Mars Express. *J. Geophys. Res.* 112 (E8), doi:10.1029/2006JE002841.
- Malin, M.C., Edgett, K.S., 2000. Sedimentary rocks of early Mars. *Science* 290 (5498), 1927–1937.
- McCullom, T.M., Hynek, B.M., 2005. A volcanic environment for bedrock diagenesis at Meridiani Planum on Mars. *Nature* 438, 1129–1131.
- McCullom, T.M., Hynek, B.M., 2007. A geochemical model for formation of Meridiani Planum layered sulfate deposits by volcanic processes. In: 7th International Conference on Mars. Abstract 1353, p. 3257.
- McCord, T.B., Orlando, T.M., Teeter, G., Hansen, G.B., Sieger, M.T., Petrik, N.G., Van Keulen, L., 2001. Thermal and radiation stability of the hydrated salt minerals epsomite, mirabilite, and natron under Europa environmental conditions. *J. Geophys. Res.* 106, 3311–3319.
- Milliken, R.E., Mustard, J.F., Poulet, F., Bibring, J., Langevin, Y., 2005. Estimating the absolute water content of Arabia Terra using Mars Express OMEGA data. In: AGU Fall Meeting 2005. Abstract #P14A-02.
- Moore, J.M., 1990. Nature of the mantling deposit in the heavily cratered terrain of northeastern Arabia, Mars. *J. Geophys. Res.* 95, 14279–14289.
- Morris, R.V., Agresti, D.G., Lauer Jr., H.V., Newcomb, J.A., Shelfer, T.D., Murali, A.V., 1989. Evidence for pigmentary hematite on Mars based on optical, magnetic, and Mössbauer studies of superparamagnetic (nanocrystalline) hematite. *J. Geophys. Res.* 94, 2760–2778.
- Morris, R.V., Ming, D.W., Golden, D.C., Bell III, J.F., 1996. An occurrence of jarositic tephra on Mauna Kea, Hawaii: Implications for the ferric mineralogy of the martian surface. In: Dyer, M.D., McCammon, C., Schaefer, M.W. (Eds.), *Mineral Spectroscopy: A Tribute to Roger G. Burns*. Spec. Publ. Geochim. Soc. 5, pp. 327–336.
- Morris, R.V., Golden, D.C., Bell, J.F., 1997. Low-temperature reflectivity spectra of red hematite and the color of Mars. *J. Geophys. Res.* 102, 9125–9134.
- Morris, R.V., and 11 colleagues, 2000. Mineralogy, composition, and alteration of Mars Pathfinder rocks and soils: Evidence from multispectral, elemental, and magnetic data on terrestrial analogue, SNC meteorite, and Pathfinder samples. *J. Geophys. Res.* 105, 1757–1817.
- Morris, R.V., and 23 colleagues, 2006. Mössbauer mineralogy of rock, soil, and dust at Meridiani Planum, Mars: Opportunity's journey across sulfate-rich outcrop, basaltic sand and dust, and hematite lag deposits. *J. Geophys. Res.* 111, doi:10.1029/2006JE002791.
- Mustard, J.F., Poulet, F., Gendrin, A., Bibring, J.-P., Langevin, Y., Gondet, B., Mangold, N., Bellucci, G., Altieri, F., 2005. Olivine and pyroxene diversity in the crust of Mars. *Science* 307 (5715), 1594–1597.
- Nelder, J.A., Mead, R., 1965. A simple method for function minimization. *Comput. J.* 7, 308–313.
- Newman, C.E., Lewis, S.R., Read, P.L., 2005. The atmospheric circulation and dust activity in different orbital epochs on Mars. *Icarus* 174, 135–160.
- Poulet, F., Cuzzi, J.N., 2002. The composition of Saturn's rings. *Icarus* 160, 350–358.
- Poulet, F., Erard, S., 2004. Nonlinear spectral mixing: Quantitative analysis of laboratory mineral mixtures. *J. Geophys. Res.* 109 (E2), doi:10.1029/2003JE002179.
- Poulet, F., Cuzzi, J.N., Cruikshank, D.P., Roush, T., Dalle Ore, C.M., 2002. Comparison between the Shkuratov and Hapke scattering theories for solid planetary surfaces: Application to the surface composition of two Centaurs. *Icarus* 160, 313–324.
- Poulet, F., Cruikshank, D.P., Cuzzi, J.N., Roush, T.L., French, R.G., 2003. Compositions of Saturn's rings A, B, and C from high resolution near-infrared spectroscopic observations. *Astron. Astrophys.* 412, 305–316.
- Poulet, F., Bibring, J.-P., Mustard, J.F., Gendrin, A., Mangold, N., Langevin, Y., Arvidson, R.E., Gondet, B., Gomez, C., 2005. Phyllosilicates on Mars and implications for early martian climate. *Nature* 438, 623–627.
- Poulet, F., Gomez, C., Bibring, J.-P., Langevin, Y., Gondet, B., Pinet, P., Bellucci, G., Mustard, J., and OMEGA team, 2007. Martian surface mineralogy from OMEGA/MEx: Global mineral maps. *J. Geophys. Res.* 112 (E8), doi:10.1029/2006JE002840. E08S02.
- Rogers, A.D., Christensen, P.R., 2007. Surface mineralogy of martian low-albedo regions from MGS-TES data: Implications for upper crustal evolution and surface alteration. *J. Geophys. Res.*, doi:10.1029/2006JE002727.
- Scott, D.H., Tanaka, K.L., 1986. Geologic map of the western equatorial region of Mars. U.S. Geological Survey Miscellaneous Investigations Series Map, I-1802-A. U.S. Geological Survey, Washington, DC.
- Schultz, P.H., Lutz, A.B., 1988. Polar wandering of Mars. *Icarus* 73, 91–141.

- Schwertmann, U., Friedl, J., Stanjek, H., 1999. From Fe(III) ions to ferrihydrite and then hematite. *J. Colloid Interface Sci.* 209, 215–223.
- Shkuratov, Y., Starukhina, L., Hoffmann, H., Arnold, G., 1999. A model of spectral albedo of particulate surfaces: Implications for optical properties of the Moon. *Icarus* 137, 235–246.
- Squyres, S.W., Knoll, A.H., 2005. Sedimentary rocks at Meridiani Planum: Origin, diagenesis, and implications for life on Mars. *Earth Planet. Sci. Lett.* 240, 1–10.
- Squyres, S.W., Grotzinger, J.P., Arvidson, R.E., Bell, J.F., Calvin, W., Christensen, P.R., Clark, B.C., Crisp, J.A., Farrand, W.H., Herkenhoff, K.E., Johnson, J.R., Klingelhöfer, G., Knoll, A.H., McLennan, S.M., McSween, H.Y., Morris, R.V., Rice, J.W., Rieder, R., Soderblom, L.A., 2004. In situ evidence for an ancient aqueous environment at Meridiani Planum, Mars. *Science* 306, 1709–1714.
- Squyres, S.W., and 19 colleagues, 2006. Planetary science: Bedrock formation at Meridiani Planum. *Nature* 443 (7107), 1–2.
- Tanaka, K.L., 2000. Dust and ice deposition in the martian geologic record. *Icarus* 144, 254–266.
- Tosca, N.J., McLennan, S.M., Lindsley, D.H., Schoonen, M.A.A., 2004. Acid-sulfate weathering of synthetic martian basalt: The acid fog model revisited. *J. Geophys. Res.* 109, doi:10.1029/2003JE002218.
- Tosca, N.J., McLennan, S.M., Clark, B.C., Grotzinger, J.P., Hurowitz, J.A., Knoll, A.H., Schröder, C., Squyres, S.W., 2005. Geochemical modeling of evaporation processes on Mars: Insight from the sedimentary record at Meridiani Planum. *Earth Planet. Sci. Lett.* 240 (1), 122–148.
- Zolotov, M.Y., Shock, E.L., 2005. Formation of jarosite-bearing deposits through aqueous oxidation of pyrite at Meridiani Planum, Mars. *Geophys. Res. Lett.* 32 (21), doi:10.1029/2005GL024253.